

# The spin Hall effect of Bi-Sb alloys driven by thermally excited Dirac-like electrons

Zhendong Chi,<sup>1,2</sup> Yong-Chang Lau,<sup>1,2,\*</sup> Xiandong Xu,<sup>2</sup> Tadakatsu

Ohkubo,<sup>2</sup> Kazuhiro Hono,<sup>2</sup> and Masamitsu Hayashi<sup>1,2,†</sup>

<sup>1</sup>*Department of Physics, The University of Tokyo,*

*Bunkyo-ku, Tokyo 113-0033, Japan*

<sup>2</sup>*National Institute for Materials Science, Tsukuba, Ibaraki 305-0047, Japan*

(Dated: October 29, 2019)

## Abstract

We have studied the charge to spin conversion in  $\text{Bi}_{1-x}\text{Sb}_x/\text{CoFeB}$  heterostructures. The spin Hall conductivity (SHC) of the sputter deposited heterostructures exhibits a high plateau at Bi-rich compositions, corresponding to the topological insulator phase, followed by a decrease of SHC for Sb-richer alloys, in agreement with the calculated intrinsic spin Hall effect of  $\text{Bi}_{1-x}\text{Sb}_x$  alloy. The SHC increases with increasing thickness of the  $\text{Bi}_{1-x}\text{Sb}_x$  alloy before it saturates, indicating that it is the bulk of the alloy that predominantly contributes to the generation of spin current; the topological surface states, if present in the films, play little role. Surprisingly, the SHC is found to increase with increasing temperature, following the trend of carrier density. These results suggest that the large SHC at room temperature, with a spin Hall efficiency exceeding 1 and an extremely large spin current mobility, is due to increased number of Dirac-like, thermally-excited electrons in the  $L$  valley of the narrow gap  $\text{Bi}_{1-x}\text{Sb}_x$  alloy.

---

\* yongchang.lau@qspin.phys.s.u-tokyo.ac.jp

† hayashi@phys.s.u-tokyo.ac.jp

## INTRODUCTION

Generation of spin current or flow of spin angular momentum lies at the heart of modern spintronics. The power consumption of a spintronic device is directly related to its efficiency for converting a charge current that dissipates energy to a dissipative spin polarized current or a dissipationless spin current[1, 2]. A conventional means for creating a flow of spin angular momentum is by passing a charge current across a ferromagnetic metal (FM) that converts to a spin polarized current. The efficacy of this process is proportional to the spin polarization of the FM. More recently, generation of spin current from a charge current passed along a non-magnetic metal (NM)[3–5] or interface of materials with strong spin orbit coupling[6–8] has emerged as an attractive alternative. In particular, the discovery[9] of the giant spin Hall effect (SHE) in  $5d$  transition heavy metals (HM) have triggered significant effort in exploiting the spin current to electrically control magnetization of ferromagnets placed nearby. In HM/FM bilayer systems, the magnetization of the FM layer can absorb the orthogonal component of the non-equilibrium spin density originating from the SHE, giving rise to current-induced spin-orbit torque (SOT) at the HM/FM interface [10–12]. The SOT in such bilayers enabled current induced magnetization switching[9, 13], current driven motion of chiral domain walls and skyrmions[14–16], and magnetoresistance effect that depends on the SHE, often referred to as the spin Hall magnetoresistance[17, 18]. The figure of merit of the charge to spin conversion in SHE is known as the damping-like spin Hall efficiency  $\xi_{DL}$  that includes non-ideal spin transmission across the interface[19, 20]. Using  $\xi_{DL}$ , the spin current  $j_s$  generated from a charge current  $j_c$  passed to a non-magnetic metal layer and entering the FM layer can be expressed as  $j_s = \xi_{DL}(\hbar/2e)j_c$  where  $\hbar$  is the reduced Planck constant and  $e$  is the electrical charge. As  $\xi_{DL}$  may depend on the longitudinal conductivity  $\sigma_{xx}$  of the NM layer which varies with extrinsic factors such as impurity concentration and film texture, it is customary to use the spin Hall conductivity (SHC)  $\sigma_{SH}$ , defined through the relation  $\sigma_{SH} = \xi_{DL} \cdot \sigma_{xx}$ , to provide a measure of the anomalous transverse velocity the carriers obtain via the SHE[5].

Recent advances in the understanding of topological insulators[21] and Weyl semimetals[22] have attracted great interest in exploiting their unique electronic states for spintronic applications. Giant charge to spin conversion efficiencies were found in heterostructures that consist of a topological insulator and a ferromagnetic/ferrimagnetic layer[23–32]. The large

charge to spin conversion efficiency observed in such systems were attributed to the current induced generation of spin density enabled by the spin momentum locked surface states of topological insulators. Ideally the bulk of a topological insulator should be insulating. In practice, however, it remains as a great challenge to limit the current flow within the bulk of this material class. This is particularly the case for thin film heterostructures in which imperfect crystal structures and interdiffusion with the adjacent layers may reduce or eliminate the band gap of the bulk state. To take advantage of the topological surface states in generating spin accumulation, it has been considered detrimental to have current paths in the bulk. In terms of bulk conduction of carriers, the charge to spin conversion efficiency of Bi, a small gap semimetal with large spin orbit coupling[33, 34] and being one of the most used elements in forming topological insulators, has been reported to be extremely small[35, 36] compared to the  $5d$  transition metals. Theoretically, Bi and Bi-Sb alloys have been predicted[37–39] to exhibit considerable SHC due to its unique electronic state.

Here, we show that the charge to spin conversion efficiency that originates from the bulk of  $\text{Bi}_{1-x}\text{Sb}_x$  alloys is significantly larger than that of the  $5d$  transition metals. The SHC of the alloy increases with increasing thickness before it saturates. Such thickness dependence of the SHC, together with its facet independence, suggest that a significant amount of spin current is generated from the bulk of the alloy: we find little evidence of spin current generation from the topological surface states, if they were to exist in the sputtered films used here. The damping-like spin Hall efficiency exceeds 1 for the Bi-rich  $\text{Bi}_{1-x}\text{Sb}_x$  alloy and decreases with increasing Sb concentration. The alloy composition dependence of the SHC indicates that the SHE of the alloy has considerable contribution from the so-called intrinsic SHE. Surprisingly, we find that the SHC and the spin Hall efficiency increases with increasing measurement temperature. We find up to three-fold (two-fold) enhancement of  $\sigma_{\text{SH}}$  ( $\xi_{\text{DL}}$ ) upon increasing the temperature from 10 K to 300 K. Although thermal fluctuation is typically detrimental for many key parameters of spintronic devices, the SHC of  $\text{Bi}_{1-x}\text{Sb}_x$  alloy is enhanced at higher temperature due to the increased number of carriers at the valleys with large Berry curvature. Our results suggest that such carriers in  $\text{Bi}_{1-x}\text{Sb}_x$  alloys, particularly in the Bi-rich compositions, possess large spin current generation efficiency and equivalent spin current mobility.

## RESULTS

### Structural characterizations

Thin film heterostructures with base structure of Sub./seed/[ $t_{\text{Bi}}$  Bi| $t_{\text{Sb}}$  Sb] $_N$ / $t_{\text{Bi}}$  Bi/ $t_{\text{CoFeB}}$  CoFeB/2 MgO/1 Ta (thicknesses in nanometer) were grown by magnetron sputtering at ambient temperature on thermally oxidized Si substrates.  $N$  represents the number of repeats of the Bi|Sb bilayers. The thicknesses of the Bi ( $t_{\text{Bi}}$ ) and Sb ( $t_{\text{Sb}}$ ) layers in the repeated structure is set to meet a condition  $t_{\text{Bi}} + t_{\text{Sb}} \sim 0.7$  nm. The nominal composition of CoFeB is Co:Fe:B=20:60:20 at%. Unless noted otherwise, we use 0.5 nm Ta as the seed layer for Bi|Sb multilayers. The capping layer is always fixed to 2 MgO/1 Ta. We assume the top 1 nm Ta layer is fully oxidized and does not contribute to the transport properties of the films.

$\theta - 2\theta$  X-ray diffraction (XRD) spectra of representative films with  $t_{\text{Bi}} \sim t_{\text{Sb}} \sim 0.35$  nm,  $N = 8, 16$  are shown in Fig. 1(a). The films are polycrystalline and the peaks are indexed based on the hexagonal representation of the rhombohedral  $\text{Bi}_{1-x}\text{Sb}_x$  (space group  $\text{R}\bar{3}\text{m}$ ; No. 166) that forms solid solution throughout the composition. Bragg diffraction peaks corresponding to (0003), (01 $\bar{1}$ 2) and (10 $\bar{1}$ 4) crystallographic directions are found. The peak intensities increase with increasing  $N$ , reflecting improved crystallinity of the film. Atomic force microscopy (AFM) image of the  $N = 8$  film is shown in Fig. 1(b). The root mean square (r.m.s.) roughness is of the order of 1 nm. Representative cross sectional high-angle annular dark-field scanning transmission electron microscopy (HAADF-STEM) images of the  $N = 16$  film are shown in Fig. 1(c). The lower magnification STEM image at the upper panel confirms that the Bi|Sb multilayer is granular and continuous. We find the average grain size is  $\sim 35$  nm. The 2 nm CoFeB and the subsequent capping layers are also continuous and follow the morphology of the multilayer. The lower panel shows the high-resolution STEM image of the film. The lattice fringes clearly seen in the image reveals the good crystallinity of Bi|Sb multilayer. A typical nanobeam diffraction pattern of the Bi|Sb multilayer is shown in the inset of Fig. 1(c). The diffraction patterns suggest that the grains are consisted of  $\text{Bi}_{1-x}\text{Sb}_x$  nanocrystallites with random orientations within the film plane. Although alternating Bi and Sb layers were sputtered to form Bi|Sb multilayers, energy-dispersive X-ray spectroscopy (EDS) mapping (see supplementary material) show

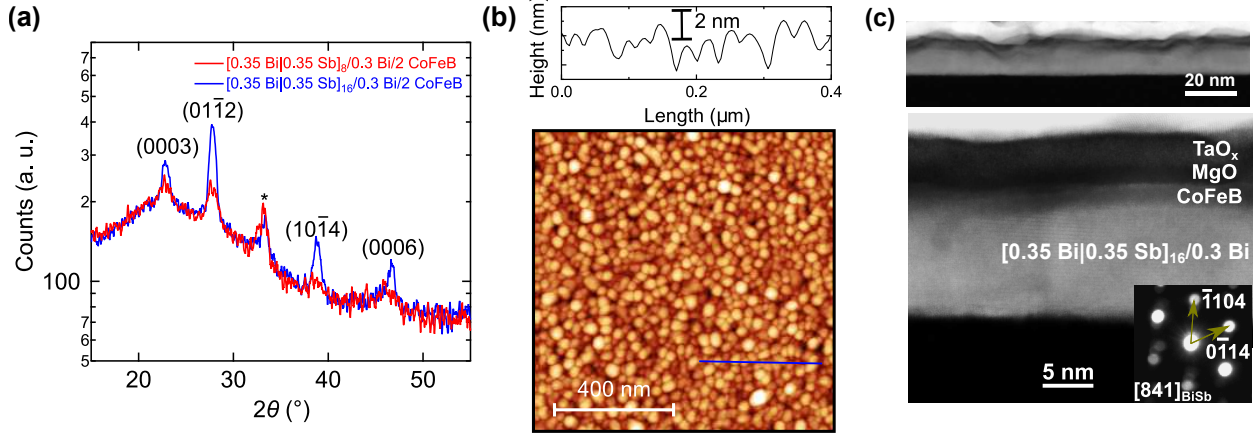


FIG. 1. **Structural characterization of Bi|Sb multilayers.** (a) X-ray diffraction (XRD) spectra of  $0.5 \text{ Ta}/[0.35 \text{ Bi}|0.35 \text{ Sb}]_N/0.3 \text{ Bi}/2 \text{ CoFeB}/2 \text{ MgO}/1 \text{ Ta}$  with  $N = 8$  (blue line) and  $N = 16$  (red line). (b) AFM image of the  $N = 8$  film. A line profile along the blue solid line drawn in the bottom image is shown at the top panel. (c) Cross-sectional HAADF-STEM images of the  $N = 16$  structure. Selected nanobeam diffraction pattern of the Bi|Sb multilayer is shown in the inset.

that the two elements intermix to form an alloy rather than a layer-by-layer superlattice.

### Experimental setup

Since structural characterization show that the two elements intermix and form an alloy, we denote, hereafter, the Bi|Sb multilayers (i.e.  $[t_{\text{Bi}} \text{ Bi}|t_{\text{Sb}} \text{ Sb}]_N/t_{\text{Bi}} \text{ Bi}$ ) as  $t_{\text{BiSb}} \text{ Bi}_{1-x}\text{Sb}_x$  using the total thickness of the multilayer ( $t_{\text{BiSb}}$ ) and the corresponding composition  $x$  defined by the relative thickness of the Bi and Sb layers, i.e.  $x \equiv \frac{t_{\text{Sb}}}{t_{\text{Bi}} + t_{\text{Sb}}}$ . To evaluate the SOT, we pattern Hall bar devices using optical lithography. The nominal channel width  $w$  and length  $L$  are set to  $10 \mu\text{m}$  and  $25 \mu\text{m}$ , respectively. Illustration of the Hall bar device and the coordinate system adapted in this work are schematically illustrated in the inset of Fig. 2(a). The longitudinal resistance  $R_{xx}$  and the transverse resistance  $R_{xy}$  of the devices were obtained using direct current (DC) transport measurements. Linear fitting to the sheet conductance  $L/(wR_{xx})$  versus the thickness of one of the layers is used to estimate the conductivity  $\sigma_X$  ( $X=\text{BiSb}, \text{CoFeB}, \text{seed layer}$ ). The current distribution within the heterostructures is calculated using the thicknesses and conductivities of the conducting

layers.

We use the harmonic Hall technique [11, 12, 40–42] to quantify the SOT of in-plane magnetized  $\text{Bi}_{1-x}\text{Sb}_x/\text{CoFeB}$  heterostructures. Upon applying an alternating current  $I_0 \sin \omega t$  with frequency  $\omega$  and amplitude  $I_0$  along  $\mathbf{x}$ , an external magnetic field  $\mathbf{H}_{\text{ext}}$  is applied in the  $xy$  plane while the in-phase first harmonic ( $V_{1\omega}$ ) and the out-of-phase second harmonic ( $V_{2\omega}$ ) Hall voltages along  $\mathbf{y}$  are simultaneously measured. The Hall resistance is obtained by dividing the harmonic voltages with  $I_0$ , *i.e.*  $R_{1\omega(2\omega)} \equiv V_{1\omega(2\omega)}/I_0$ .  $R_{1\omega}$  is dominated by the planar Hall and anomalous Hall resistances, whereas  $R_{2\omega}$  contains contributions from current-induced damping-like spin-orbit effective field ( $H_{\text{DL}}$ ), the field-like spin-orbit effective field ( $H_{\text{FL}}$ ), the Oersted field ( $H_{\text{Oe}}$ ) and thermoelectric effects (anomalous Nernst effect (ANE) of CoFeB, the ordinary Nernst effect (ONE) of  $\text{Bi}_{1-x}\text{Sb}_x$ [43], and the collective action of the spin Seebeck effect (SSE) in CoFeB followed by the inverse spin Hall effect (ISHE) in  $\text{Bi}_{1-x}\text{Sb}_x$ [41]). The magnetic field amplitude dependence of  $R_{2\omega}$  allows one to differentiate contributions from each effect: see MATERIALS AND METHODS for the details.  $H_{\text{DL}}$  ( $H_{\text{FL}}$ ) is related to the damping-like (field-like) spin Hall efficiency via  $\xi_{\text{DL(FL)}} = \frac{2e}{\hbar} \frac{H_{\text{DL(FL)}} M_s t_{\text{eff}}}{j_{\text{BiSb}}}$ , where  $j_{\text{BiSb}}$  is the current density in  $\text{Bi}_{1-x}\text{Sb}_x$ ,  $M_s$  and  $t_{\text{eff}} \equiv t_{\text{CoFeB}} - t_{\text{D}}$  denote the saturation magnetization and the effective thickness of the CoFeB layer.  $t_{\text{D}}$  is the thickness of the magnetic dead layer (see supplementary materials for details of magnetic properties of the films). From hereon, we discuss the values of  $\xi_{\text{DL}}$  and  $\xi_{\text{FL}}$ . To estimate the spin Hall conductivity of  $\text{Bi}_{1-x}\text{Sb}_x$ , we use the relation  $\sigma_{\text{SH}} = \xi_{\text{DL}} \sigma_{\text{BiSb}}$ , where the spin transmission across the  $\text{Bi}_{1-x}\text{Sb}_x/\text{CoFeB}$  interface is assumed transparent[19, 20, 44]. Taking into account a non-transparent interface will result in larger  $\xi_{\text{DL}}$  (and likely  $\xi_{\text{FL}}$ ) and therefore results in larger  $\sigma_{\text{SH}}$ .

### **BiSb thickness dependence of $\sigma_{\text{SH}}$**

We first study the layer thickness dependence of the transport properties of heterostructures with nearly equiatomic  $\text{Bi}_{0.53}\text{Sb}_{0.47}$  ( $t_{\text{Bi}} \sim t_{\text{Sb}} \sim 0.35$  nm). The conductivity of  $\text{Bi}_{0.53}\text{Sb}_{0.47}$  is plotted against  $t_{\text{BiSb}}$  in Fig. 2(a). The slight increase of  $\sigma_{\text{BiSb}}$  with  $t_{\text{BiSb}}$  may be related to the larger grain size of thicker films that reduces the scattering at grain boundaries. Note that  $\sigma_{\text{CoFeB}}$  takes an average value of  $\sim 5.5 \times 10^3 \Omega^{-1} \text{cm}^{-1}$  and shows little dependence on  $t_{\text{BiSb}}$ . The  $t_{\text{BiSb}}$  dependence of  $\xi_{\text{DL}}$  and  $\xi_{\text{FL}}$  for  $\text{Bi}_{0.53}\text{Sb}_{0.47}/\text{CoFeB}$

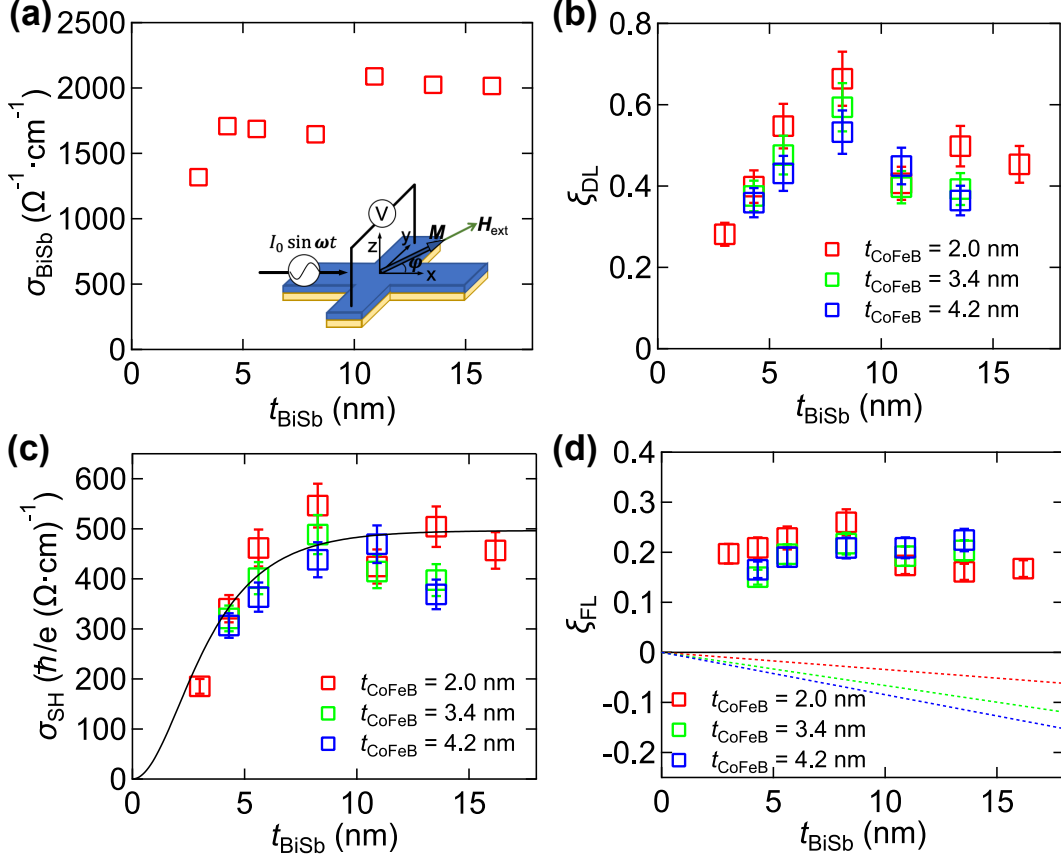


FIG. 2.  $\text{Bi}_{0.53}\text{Sb}_{0.47}$  thickness dependence of SOT and  $\sigma_{\text{SH}}$ . (a) The conductivity  $\sigma_{\text{BiSb}}$  of  $\text{Bi}_{0.53}\text{Sb}_{0.47}$  plotted as a function of its thickness  $t_{\text{BiSb}}$ . Inset: schematic illustration of a Hallbar device and the coordinate system. (b-d)  $t_{\text{BiSb}}$  dependence of the damping-like spin Hall efficiency  $\xi_{\text{DL}}$  (b), the spin Hall conductivity  $\sigma_{\text{SH}}$  (c) and the field-like spin Hall efficiency  $\xi_{\text{FL}}$  (d) of  $t_{\text{BiSb}}$   $\text{Bi}_{0.53}\text{Sb}_{0.47}/t_{\text{CoFeB}}$  CoFeB. Dotted lines represent contributions from the Oersted field. All data were obtained at 300 K.

heterostructures measured at 300 K are shown in Fig. 2(b) and 2(d), respectively. For a given  $t_{\text{BiSb}}$ , we studied devices with three different  $t_{\text{CoFeB}}$  ( $\sim 2, 3.4$ , and  $4.3$  nm). We find  $\xi_{\text{DL}}$  of  $\text{Bi}_{0.53}\text{Sb}_{0.47}$  is of the same sign with that of Pt [45] and is consistent with previous reports on MBE-grown  $\text{Bi}_{0.9}\text{Sb}_{0.1}$  [31] and stoichiometric  $\text{Bi}_2\text{Se}_3$  [23, 29] topological insulators. At  $t_{\text{BiSb}} \sim 8$  nm,  $\xi_{\text{DL}}$  reaches a maximum of  $\sim 0.65$ . This value is significantly larger than those found in heavy metals but lower than some recent reports on Bi-based topological insulators [23, 28, 30, 31].  $\xi_{\text{DL}}$  shows little dependence on  $t_{\text{CoFeB}}$ , indicating that the CoFeB layer plays little role in setting the SOT of the heterostructures. In order to take into account the change of  $\sigma_{\text{BiSb}}$  with  $t_{\text{BiSb}}$ , we plot the spin Hall conductivity  $\sigma_{\text{SH}} = \xi_{\text{DL}}\sigma_{\text{BiSb}}$  against  $t_{\text{BiSb}}$

in Fig. 2(c).  $\sigma_{\text{SH}}$  increases with increasing  $t_{\text{BiSb}}$  and tends to saturate beyond  $t_{\text{BiSb}}$  of  $\sim 8$  nm. Such thickness dependence resembles that expected for the bulk SHE in  $\text{Bi}_{0.53}\text{Sb}_{0.47}$  and is inconsistent with the surface-state-dominant scenario [23, 46] nor with the quantum confinement picture [30]. We fit all data using the relation  $\sigma_{\text{SH}} = \bar{\sigma}_{\text{SH}}[1 - \text{sech}(\frac{t_{\text{BiSb}}}{\lambda})]$  with the *bulk* spin Hall conductivity  $\bar{\sigma}_{\text{SH}}$  and the spin diffusion length  $\lambda$  as the fitting parameters[47]. We find  $\bar{\sigma}_{\text{SH}} = 496 \pm 26$  ( $\hbar/e$ ) $\Omega^{-1}\text{cm}^{-1}$  and  $\lambda = 2.3 \pm 0.4$  nm for  $\text{Bi}_{0.53}\text{Sb}_{0.47}$ .

Figure 2(d) illustrates the  $t_{\text{BiSb}}$  dependence of  $\xi_{\text{FL}}$  for heterostructures with different CoFeB thicknesses. The contribution from  $H_{\text{Oe}}$ , which takes the form of  $H_{\text{Oe}}/j_{\text{BiSb}} = 2\pi t_{\text{BiSb}}$  ( $10^{-1}$  Oe/(A $\cdot$ cm $^{-2}$ )) according to the Ampère's law, is shown by the dotted lines in Fig. 2(d). Note that  $H_{\text{Oe}}$ , being negative in our convention, is subtracted from the total field-like SOT to calculate  $\xi_{\text{FL}}$ . We find  $H_{\text{FL}}$  is opposite to the Oersted field and  $\xi_{\text{FL}}$  takes a constant value of  $\sim 0.2$  throughout the range of  $t_{\text{BiSb}}$  studied. The sign of  $\xi_{\text{FL}}$  for  $\text{Bi}_{0.53}\text{Sb}_{0.47}/\text{CoFeB}$  agrees with that of metallic Pt/Co/AlO $_x$ [12], while being opposite to that found in  $\text{Bi}_2\text{Se}_3/\text{NiFe}$  [23] and in  $\text{MoS}_2/\text{CoFeB}$ [48]. The nearly constant  $\xi_{\text{FL}}$  against  $t_{\text{BiSb}}$  is observed for all structures with different  $t_{\text{CoFeB}}$ . The distinct  $t_{\text{BiSb}}$  dependence of  $\xi_{\text{FL}}$  and  $\xi_{\text{DL}}$  suggests the two orthogonal components of SOT originate from phenomena of different characteristic length scales[11, 49].

### **$\text{Bi}_{1-x}\text{Sb}_x$ composition and facet dependence of $\sigma_{\text{SH}}$**

Bulk  $\text{Bi}_{1-x}\text{Sb}_x$  alloy is known to be a semiconductor with a small band gap hosting topological surface states for  $0.09 \leq x \leq 0.22$  and is semimetallic for the other compositions[33, 34, 50, 51]. In an effort to shed light on the origin of the SOT, we investigate the Sb concentration ( $x$ ) dependence of  $\sigma_{\text{SH}}$  and related parameters in 10  $\text{Bi}_{1-x}\text{Sb}_x/2$  CoFeB heterostructures. To characterize the basic transport properties of  $\text{Bi}_{1-x}\text{Sb}_x$  alloy, stacks without the CoFeB layer (*i.e.*  $t_{\text{CoFeB}} = 0$ ) were also deposited and measured. We have excluded pure Bi ( $x = 0$ ) from this study due to its large sheet resistance (considerably larger than those of the  $x \neq 0$  alloys) and island-like morphology which may result in highly non-uniform current flow within the CoFeB layer. For alloys with  $x > 0$ , the surface roughness significantly improves, as shown in Fig. 1(b). Figure 3(a) shows the  $x$  dependence of  $\sigma_{\text{BiSb}}$ :  $\sigma_{\text{BiSb}}$  increases monotonically with increasing Sb concentration. This is consistent with previous report on the transport properties of bulk  $\text{Bi}_{1-x}\text{Sb}_x$  alloy[50], where it was shown that  $\text{Bi}_{1-x}\text{Sb}_x$

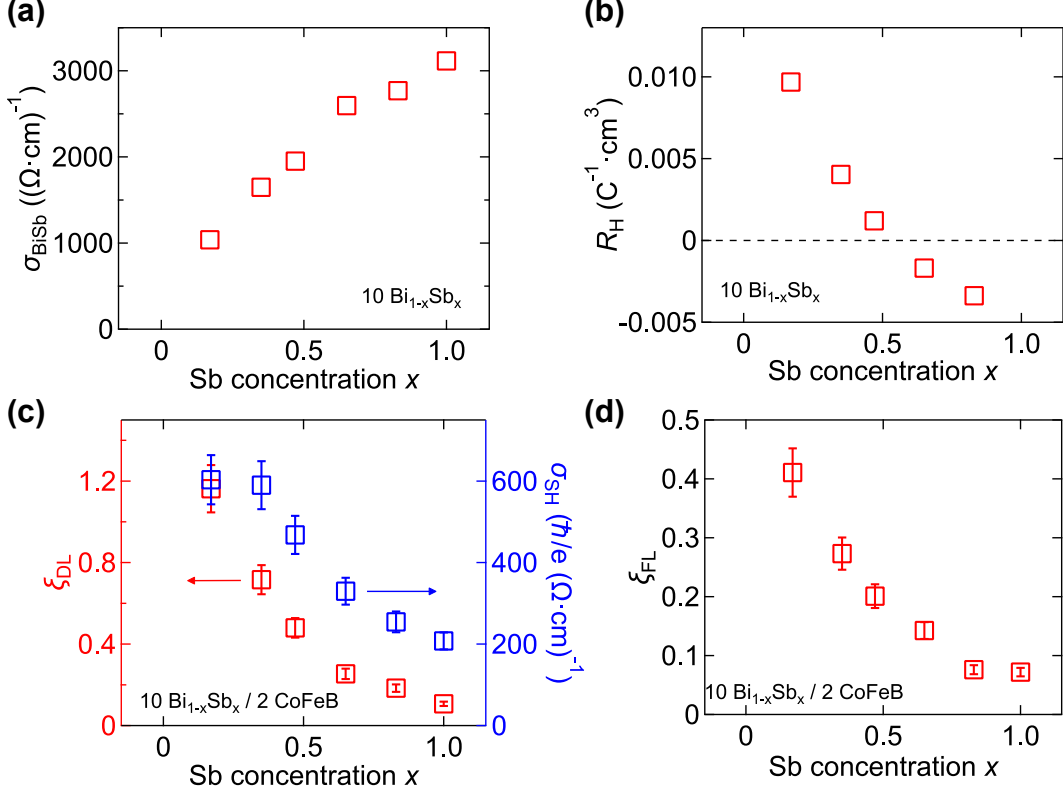


FIG. 3. **Bi<sub>1-x</sub>Sb<sub>x</sub> composition dependence of carrier transport and  $\sigma_{\text{SH}}$ .** (a,b) Sb composition  $x$  dependence of the conductivity  $\sigma_{\text{BiSb}}$  (a) and the Hall coefficient  $R_{\text{H}}$  (b) of Bi<sub>1-x</sub>Sb<sub>x</sub> with  $t_{\text{BiSb}} = 10$  nm. For these studies, heterostructures without the CoFeB layer was used. (c,d) Sb concentration ( $x$ ) dependence of the damping-like spin Hall efficiency  $\xi_{\text{DL}}$  (left axis), the spin Hall conductivity  $\sigma_{\text{SH}}$  (right axis) (c), and the field-like spin Hall efficiency  $\xi_{\text{FL}}$  (d) for 10 Bi<sub>1-x</sub>Sb<sub>x</sub>/2 CoFeB heterostructures. All data were collected at 300 K.

gradually changes from being a semiconductor to a semimetal with increasing Sb concentration. As shown in Fig. 3(b), the ordinary Hall coefficient  $R_{\text{H}} \equiv R_{xy}t_{\text{BiSb}}/H_z$  ( $H_z$  is the external field  $H_{\text{ext}}$  along  $z$ ) also varies monotonically with increasing  $x$ . In our convention,  $R_{\text{H}} > 0$  ( $R_{\text{H}} < 0$ ) corresponds to carrier transport being dominated by electrons (holes). We find the carriers of Bi-rich alloys are electron-dominant whereas the Sb-rich structures are hole-dominant, accompanied by a smooth sign change of  $R_{\text{H}}$  at  $x \sim 0.55$ . This reflects the multi-carrier nature of the polycrystalline Bi<sub>1-x</sub>Sb<sub>x</sub> films, having at least a hole and an electron pocket at the Fermi level. We note that this differs from the ternary (Bi<sub>1-x</sub>Sb<sub>x</sub>)<sub>2</sub>Te<sub>3</sub> topological insulator for which  $R_{\text{H}}$  diverges and abruptly changes sign when traversing the Dirac point[26].

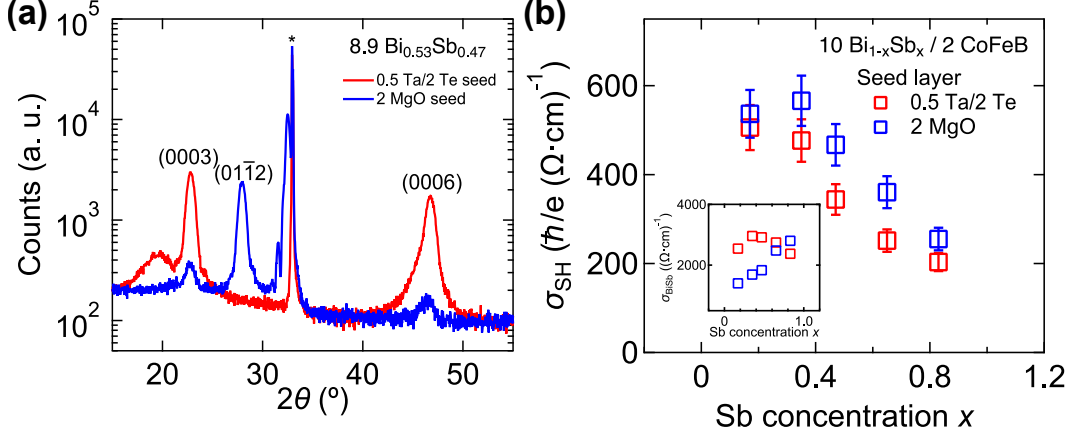


FIG. 4. **Facet dependence of  $\sigma_{\text{SH}}$ .** (a) X-ray diffraction (XRD) spectra for 8.9  $\text{Bi}_{0.53}\text{Sb}_{0.47}$  grown on 0.5 Ta/2 Te (red) and 2 MgO (blue) seed layers. Heterostructures without the CoFeB layer was used. (b) Sb concentration ( $x$ ) dependence of spin Hall conductivity  $\sigma_{\text{SH}}$  for 10  $\text{Bi}_{1-x}\text{Sb}_x/2$  CoFeB heterostructures with the two seed layers described in (a). The inset shows the  $x$  dependence of  $\sigma_{\text{BiSb}}$ . The measurement temperature is 300 K.

$\xi_{\text{DL}}$ ,  $\sigma_{\text{SH}}$ , and  $\xi_{\text{FL}}$  as a function of  $x$  for  $\text{Bi}_{1-x}\text{Sb}_x/2$  CoFeB heterostructures are presented in Figs. 3(c) and 3(d).  $\xi_{\text{DL}}$  and  $\xi_{\text{FL}}$  increase with increasing Bi concentration, reaching a maximum of  $\xi_{\text{DL}} \sim 1.2$  and  $\xi_{\text{FL}} \sim 0.41$  for structures with  $x \sim 0.17$ , a composition for which bulk  $\text{Bi}_{1-x}\text{Sb}_x$  is commonly classified as a topological insulator. However, we emphasize that the BiSb thickness dependence in the previous section and the facet dependence of SHE in the next paragraph both suggest the bulk origin of the SHE. The  $x$  dependence of  $\sigma_{\text{SH}}$  exhibits similar trend with that of  $\xi_{\text{DL}}$ : we find a plateau of  $\sigma_{\text{SH}} \sim 600(\hbar/e)\Omega^{-1}\text{cm}^{-1}$  for  $x < 0.35$ . Interestingly, such  $x$  dependence of  $\sigma_{\text{SH}}$  is in very good agreement with that obtained from tight binding calculations[38], suggesting the dominance of the intrinsic contribution over that of the extrinsic skew scattering and side-jump contributions for the observed SHE in  $\text{Bi}_{1-x}\text{Sb}_x$ .

We have also varied the seed layer of the  $\text{Bi}_{1-x}\text{Sb}_x$  layer to study the facet-dependent SHE. Figure 4(a) shows the XRD spectra of 8.9 nm thick  $\text{Bi}_{0.53}\text{Sb}_{0.47}$  films grown on different seed layers, showing that the orientation of  $\text{Bi}_{0.53}\text{Sb}_{0.47}$  nanocrystallites can be tuned from being practically random ( $\text{Bi}_{0.53}\text{Sb}_{0.47}$  on 0.5 Ta seed; c.f. Fig.1(a)) to strongly (0003)-oriented (0.5 Ta/2 Te seed) or strongly (01 $\bar{1}$ 2)-oriented (2 MgO seed). The Sb concentration ( $x$ ) dependence of the longitudinal conductivity  $\sigma_{\text{BiSb}}$  and the SHC of  $\text{Bi}_{1-x}\text{Sb}_x$  are shown

in Fig. 4(b). As evident from the inset of Fig. 4(b), difference in the texture causes large changes in  $\sigma_{\text{BiSb}}$ , particularly at smaller  $x$ . Interestingly, however, the  $x$  dependence of SHC (Fig. 4(b)) hardly changes upon varying the  $\text{Bi}_{1-x}\text{Sb}_x$  texture and  $\sigma_{\text{BiSb}}$ . We thus infer that topological surface states, which are intimately related to the  $\text{Bi}_{1-x}\text{Sb}_x$  facets [52], are therefore unlikely to be the primary source of the observed SHE. The robustness of SHC against  $\sigma_{\text{BiSb}}$  further consolidates our suggestion that the intrinsic mechanism can account for the observed SHE.

### Temperature dependence of $\sigma_{\text{SH}}$

Finally, we examine the temperature dependence of the transport properties for  $\text{Bi}_{1-x}\text{Sb}_x/\text{CoFeB}$  heterostructures with selected  $x$  ( $x \sim 0.17, 0.47$  and  $0.65$ ). Here the seed layer of  $\text{Bi}_{1-x}\text{Sb}_x$  is 0.5 nm Ta. Figure 5(a) shows  $\sigma_{\text{BiSb}}$  as a function of the measurement temperature. We find  $\text{Bi}_{1-x}\text{Sb}_x$  possesses weak and positive temperature coefficient of the conductance, being typical for a semiconductor. To obtain the variation of the carrier concentration and mobility of  $\text{Bi}_{1-x}\text{Sb}_x$ , temperature dependence of the longitudinal magnetoresistance (MR) ratio  $((R_{\text{xx}}(H_z) - R_{\text{xx}}(H_z = 0))/R_{\text{xx}}(H_z = 0))$  and  $R_{\text{xy}}$  were measured against  $H_z$ . Within the framework of a two-band model[53], we define  $n_{\text{h}}$  ( $n_{\text{e}}$ ) as the effective hole (electron) concentration of  $\text{Bi}_{1-x}\text{Sb}_x$ , with an effective mobility  $\mu_{\text{h}}$  ( $\mu_{\text{e}}$ ). Assuming equal population of the two carriers ( $n_{\text{h}} = n_{\text{e}} = n$ )[51], we evaluate these parameters for temperatures ranging from 50 K to 300 K, where the MR ratio and  $R_{\text{xy}}$  are respectively quadratic and linear with  $H_z$  up to 8 T (see supplementary materials for details of two-band model analysis). The temperature dependence of the carrier concentration and the mobility are summarized in Figs. 5(b-d). The carrier concentration increases with increasing temperature, which we infer is caused by the thermal broadening of the Fermi-Dirac distribution. In contrast,  $\mu_{\text{h}}$  and  $\mu_{\text{e}}$  both decrease with increasing temperature, obeying a power law that scales with  $\sim T^{-0.5}$ . These results indicate a competition between the impurity-mediated ( $\propto T^{1.5}$ ) and electron-phonon scattering ( $\propto T^{-1.5}$ ), with the latter being more dominant. Compared to the carrier concentration and mobility of the majority carrier for bulk single-crystal Bi ( $n \sim 4.6 \times 10^{17} \text{ cm}^{-3}$ ;  $\mu_{\text{e}} \sim 6 \times 10^5 \text{ cm}^2 \text{ V}^{-1} \text{ s}^{-1}$ )[54] and Sb ( $n \sim 3.9 \times 10^{19} \text{ cm}^{-3}$ ;  $\mu_{\text{h}} \sim 2 \times 10^4 \text{ cm}^2 \text{ V}^{-1} \text{ s}^{-1}$ )[55] at 77 K,  $n$  of the  $\text{Bi}_{1-x}\text{Sb}_x$  films studied here are one to two orders of magnitude higher while  $\mu$  are orders of magnitude lower. These are expected for sputtered polycrystalline thin films

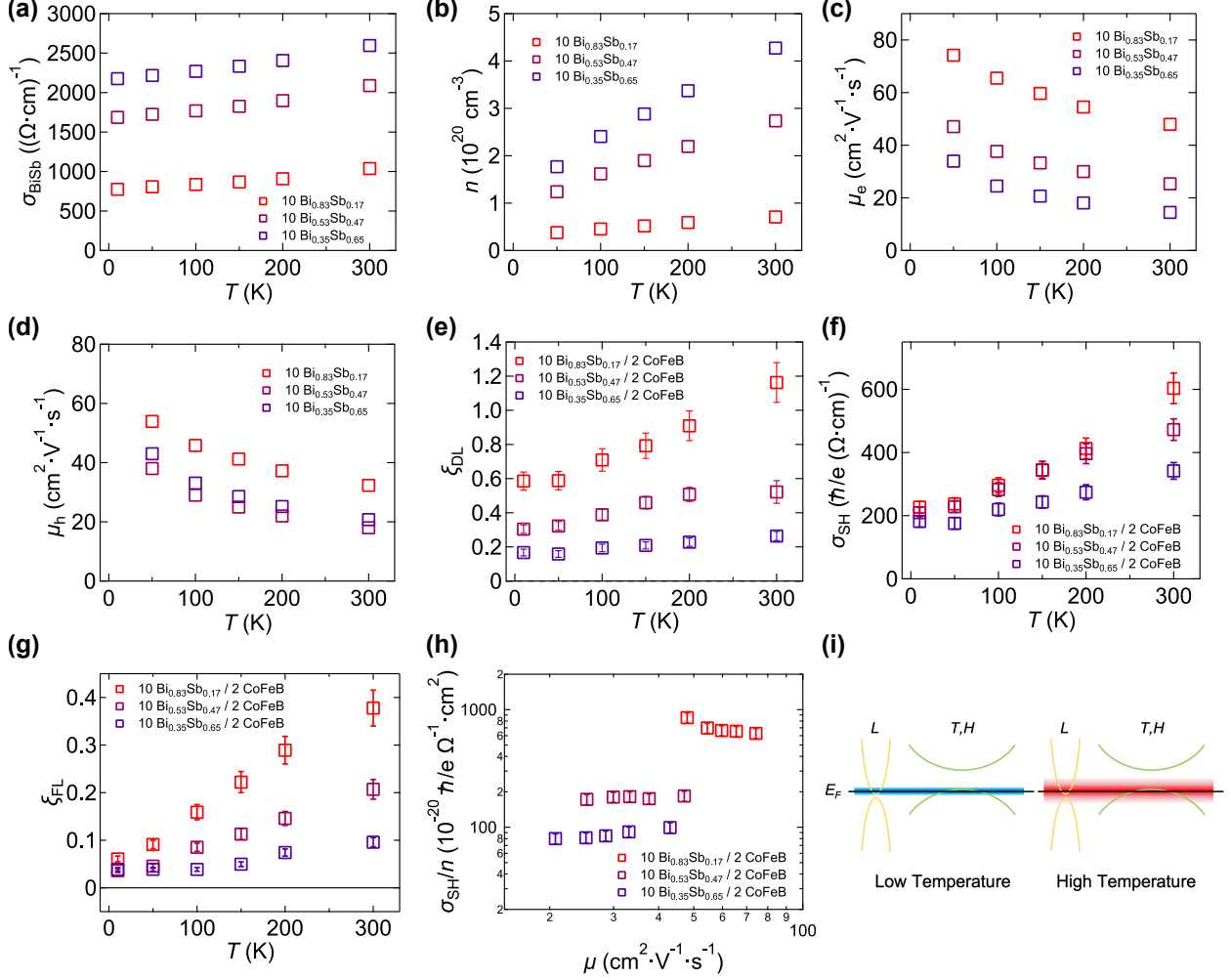


FIG. 5. **Temperature dependence of carrier transport and  $\sigma_{\text{SH}}$ .** (a-c) Temperature dependence of the conductivity  $\sigma_{\text{BiSb}}$  (a), the effective carrier concentration  $n$  (b), the electron mobility  $\mu_e$  (c), and the hole mobility  $\mu_d$  (c) for 10 Bi<sub>1-x</sub>Sb<sub>x</sub>. Heterostructures without the CoFeB layer were used. (e-g) Temperature dependence of the damping-like spin Hall efficiency  $\xi_{\text{DL}}$  (e), the spin Hall conductivity  $\sigma_{\text{SH}}$  (f), and the field-like spin Hall efficiency  $\xi_{\text{FL}}$  (g) for 10 Bi<sub>1-x</sub>Sb<sub>x</sub>/2 CoFeB heterostructures. (h)  $\sigma_{\text{SH}}/n$  as a function of the majority carrier mobility ( $\mu_e$  for  $x=0.17$ ,  $0.47$  and  $\mu_h$  for  $x=0.65$ ) 10 Bi<sub>1-x</sub>Sb<sub>x</sub>/2 CoFeB heterostructures. (i) Schematic illustration of the band structures of Bi-rich Bi<sub>1-x</sub>Sb<sub>x</sub> alloy with thermal broadening at low and high temperatures.

that contain significantly higher defect density compared to that of the bulk samples[36].

The temperature dependence of  $\xi_{\text{DL}}$ ,  $\sigma_{\text{SH}}$  and  $\xi_{\text{FL}}$  for 10 Bi<sub>1-x</sub>Sb<sub>x</sub>/2 CoFeB heterostructures are plotted in Figs. 5(e), (f) and (g) respectively. Surprisingly, all these quantities strongly enhance upon increasing the temperature from 10 K to room temperature (300 K),

suggesting that such enhancement is a rather generic feature for  $\text{Bi}_{1-x}\text{Sb}_x$  alloy. Notably for  $\text{Bi}_{0.83}\text{Sb}_{0.17}$ , up to a three-fold (two-fold) enhancement is observed for  $\sigma_{\text{SH}}$  ( $\xi_{\text{DL}}$ ) over the investigated temperature interval. While similar increase of  $\xi_{\text{FL}}$  with increasing temperature was previously reported in HM/FM heterostructures[49, 56], such strong enhancement of technologically-important  $\xi_{\text{DL}}$  and  $\sigma_{\text{SH}}$  with increasing temperature has not been observed in metallic systems. We have also studied the temperature dependence of  $\sigma_{\text{SH}}$  for thinner  $\text{Bi}_{1-x}\text{Sb}_x$  films (5.6  $\text{Bi}_{0.53}\text{Sb}_{0.47}/2$  CoFeB). We find similar temperature dependence of  $\sigma_{\text{SH}}$  compared to that shown in Fig. 5(e), which suggests that the temperature dependence of  $\xi_{\text{DL}}$ ,  $\sigma_{\text{SH}}$  and  $\xi_{\text{FL}}$  is not due to a temperature dependent spin diffusion length of  $\text{Bi}_{1-x}\text{Sb}_x$ . We have also verified that the CoFeB magnetization hardly changes within this temperature range (see supplementary materials), reassuring that the change of  $\xi_{\text{DL}}$  and  $\xi_{\text{FL}}$  with temperature is caused by the modulation of the injected spin current.

## DISCUSSION

Within the Drude model, the longitudinal conductivity  $\sigma_{\text{BISb}}$  is proportional to the carrier concentration  $n$  and the mobility  $\mu$ .  $\mu$  is proportional to the relaxation time  $\tau$  since  $\mu = e\tau/m^*$  where  $m^*$  is the effective mass. On varying the temperature, contribution from  $n$  surpasses that of  $\mu$  in  $\text{Bi}_{1-x}\text{Sb}_x$ , resulting in a positive temperature coefficient of the conductance, as shown in Fig. 5(a). For the SHC, by definition, the relaxation time dependence of  $\sigma_{\text{SH}}$  provides a measure of the mechanism of the SHE:  $\sigma_{\text{SH}} \sim \tau^1$  for the extrinsic skew scattering and  $\sigma_{\text{SH}} \sim \tau^0$  when the intrinsic or side-jump mechanism dominates[5]. With regard to the relation between  $\sigma_{\text{SH}}$  and  $n$ , the intrinsic contribution should scale with  $n$  if the analogy with the anomalous Hall conductivity applies[2]. Calculations suggest that similar scaling between  $\sigma_{\text{SH}}$  and  $n$  holds for the extrinsic mechanisms[57]. We may thus take the ratio  $\sigma_{\text{SH}}/n$  to eliminate the effect of  $n$  on the temperature dependence of  $\sigma_{\text{SH}}$ :  $\sigma_{\text{SH}}/n$  must be proportional to  $\mu^1$  for the extrinsic skew scattering mechanism and is a constant for the intrinsic/side-jump mechanism. Figure 5(h) shows  $\sigma_{\text{SH}}/n$  as a function of the mobility  $\mu$  (here the mobility of the majority carrier is used, *i.e.*,  $\mu_e$  for  $x=0.17, 0.47$  and  $\mu_h$  for  $x=0.65$ ). We find a relatively weak mobility dependence of  $\sigma_{\text{SH}}/n$  for all alloy compositions studied. The slope of  $\sigma_{\text{SH}}/n$  vs.  $\mu$  tends to increase as the Sb concentration increases. These results indicate that the extrinsic skew scattering contribution is relatively weak for Bi-rich alloys

with large intrinsic SHE but this contribution becomes non-negligible (but still smaller than the intrinsic one) with increasing  $x$  (and  $\sigma_{\text{BiSb}}$ ). Although this is reminiscent of the crossover from intrinsic to extrinsic SHE for metallic Pt upon tuning the resistivity of the metal[58], we note that  $\sigma_{\text{BiSb}}$  at the crossover is one to two orders of magnitude lower than that of Pt. Alternatively, we consider this crossover is a consequence of the band structure modification induced by Sb doping. As shown in the schematic band structure Fig.5(i), the transport in Bi-rich  $\text{Bi}_{1-x}\text{Sb}_x$  alloy is dominated by the Dirac-like electrons at the  $L$ -point in the momentum space[33, 34, 37, 50, 51]. Upon substituting Bi with Sb, holes from the  $T$  and  $H$  points with quadratic-like dispersion become increasingly important for the conduction, as shown by the  $x$ -dependence of  $R_{\text{H}}$  in Fig. 3(b). Our experimental results indicate that Dirac-like  $L$ -electrons, in contrast to holes in  $T$  and  $H$ -pockets with quadratic dispersion, is the key for achieving large intrinsic SHE in  $\text{Bi}_{1-x}\text{Sb}_x$ . We thus consider the large enhancement of SHC with temperature is caused by the increased number of  $L$ -electrons due to thermal broadening of the Fermi-Dirac distribution.

Referring to the relation between the carrier density, mobility and conductivity that derives from the Drude model,  $\sigma_{\text{SH}}/n$  can be regarded as the equivalent carrier mobility of transverse spin current. To provide reference of the equivalent mobility, we estimate  $\sigma_{\text{SH}}/n$  of a typical transition metal, Pt, which has the highest intrinsic spin Hall conductivity reported thus far ( $\sigma_{\text{SH}} \approx 2000 (\hbar/e)\Omega^{-1}\text{cm}^{-1}$  at 0 K[59]). Assuming the carrier density  $n$  of Pt is of the order of  $10^{22} \text{ cm}^{-3}$ , we obtain  $\sigma_{\text{SH}}/n \sim 20 \times 10^{-20} (\hbar/e)\Omega^{-1}\text{cm}^2$ . This is more than an order of magnitude smaller than that of  $\text{Bi}_{0.83}\text{Sb}_{0.17}$  evaluated at room temperature ( $\sigma_{\text{SH}}/n \sim 800 \times 10^{-20} (\hbar/e)\Omega^{-1}\text{cm}^2$ ). The difference is also significant within the  $\text{Bi}_{1-x}\text{Sb}_x$  alloy. If we compare  $\text{Bi}_{0.83}\text{Sb}_{0.17}$  with  $\text{Bi}_{0.35}\text{Sb}_{0.65}$ , although the spin Hall conductivity  $\sigma_{\text{SH}}$  differs by a factor of two, the equivalent mobility  $\sigma_{\text{SH}}/n$  is larger for the former by nearly one order of magnitude. These results demonstrate the exceptionally high spin current generation efficiency and mobility of the Dirac-like  $L$ -electrons in Bi-rich BiSb alloys compared to the majority holes in Sb-rich BiSb and the predominantly  $s$ -like conduction electrons in Pt.

In summary, we have studied the spin orbit torque (SOT) in sputter-deposited  $\text{Bi}_{1-x}\text{Sb}_x/\text{CoFeB}$  heterostructures. The spin Hall conductivity (SHC) of  $\text{Bi}_{1-x}\text{Sb}_x$  increases with increasing thickness until saturation and is facet independent. These results suggest a dominant contribution from the bulk of the alloy: the effect of the topological surface states, if any, is

not evident. The SHC is the largest with Bi-rich composition and decreases with increasing Sb concentration. Such trend is in accordance with the intrinsic spin Hall effect of  $\text{Bi}_{1-x}\text{Sb}_x$  predicted using tight binding calculations. Interestingly, the SHC and the damping-like spin Hall efficiency increase with increasing temperature. For example, the damping-like spin Hall efficiency of  $\text{Bi}_{0.83}\text{Sb}_{0.17}$  exhibits a two-fold enhancement from 5 K to room temperature, reaching  $\xi_{\text{DL}} \sim 1.2$ . We infer that thermally-excited population of the Dirac-like electrons in the  $L$  valley of the narrow gap  $\text{Bi}_{1-x}\text{Sb}_x$  is responsible for the temperature dependent SOT. These results show that the Dirac-like electrons in Bi-rich  $\text{Bi}_{1-x}\text{Sb}_x$  alloys are extremely effective in generating spin current and their equivalent spin current mobility is more than an order of magnitude larger than that of typical transition metals with strong spin orbit coupling. The very high spin Hall efficiency of Bi-rich  $\text{Bi}_{1-x}\text{Sb}_x$  makes this material an outstanding candidate for applications involving spin current generation and detection at elevated temperatures. In addition, the lower carrier concentration and therefore a smaller electric-field screening length in  $\text{Bi}_{1-x}\text{Sb}_x$  compared to the common heavy metals allow efficient electric field control of SOT, thus paving a route to multifunctional spinorbitronic devices being sensitive to external stimuli such as heat and electric field.

## MATERIALS AND METHODS

### Sample preparation and characterization

All samples were grown at ambient temperature by magnetron sputtering on Si substrates ( $10 \times 10 \text{ mm}^2$ ) coated with 100 nm thick thermally oxidized Si layer. Atomic force microscopy (AFM) were used to characterize the roughness of the surface.  $\theta - 2\theta$  X-ray diffraction (XRD) spectra were obtained using a Cu  $K\alpha$  source in parallel beam configuration and with a graphite monochromator on the detector side. The saturation magnetization and the magnetic dead layer thickness of the CoFeB layer in the heterostructures were determined by hysteresis loop measurements using vibrating sample magnetometer (VSM). AFM, XRD and VSM studies were performed using unpatterned constant thickness films. High-angle annular dark-field scanning transmission electron microscopy (HAADF-STEM) analysis of cross-sectioned samples were performed using a FEI Titan G2 80-200 transmission electron microscope (TEM) with a probe forming spherical aberration corrector operated at

200 kV. The samples were cross-sectioned from a plain film into thin lamellae by focused ion beam (FIB) lift-out technique using FEI Helios G4 UX. Hall bars for the transport measurements were patterned from the films using optical lithography and Ar ion etching. The width  $w$  and the distance between the two longitudinal voltage probes  $L$  are 10  $\mu\text{m}$  and 25  $\mu\text{m}$ , respectively. Contact pads to the Hall bars, 10 Ta /100 Au (thickness in nm), were formed using a standard lift-off processes.

### SOT measurements

We treat the CoFeB magnetization as a spin domain magnet with a magnetization vector  $\mathbf{M}$  lying in the film plane ( $xy$  plane) at equilibrium. The external magnetic field  $\mathbf{H}_{\text{ext}}$  is applied along the film plane with an angle  $\varphi_H$  with respect to the  $x$  axis. We assume the in-plane magnetic anisotropy of the CoFeB layer is negligible compared to the magnitude of  $\mathbf{H}_{\text{ext}}$ . Thus the angle  $\varphi$  between  $\mathbf{M}$  and the  $x$  axis is assumed be equal to  $\varphi_H$ .

When current is passed along  $\mathbf{x}$ , electrons with their spin direction parallel to  $\mathbf{y}$  diffuses into the CoFeB layer via the spin Hall effect. The impinging spin current exerts spin-transfer torque (or often referred to as the spin-orbit torque) on the CoFeB magnetization. The torque can be decomposed into two components, the damping-like and field-like torques: the equivalent effective fields are defined as  $H_{\text{DL}}$  and  $H_{\text{FL}}$ , respectively. Together with the Oersted field  $H_{\text{Oe}}$ ,  $H_{\text{DL}}$  and  $H_{\text{FL}}$  cause tilting of the CoFeB layer magnetization. When an ac current (amplitude  $I_0$ , frequency  $\omega/2\pi$ ) is applied to the heterostructure, current-induced oscillation of  $\mathbf{M}$  leads to Hall voltage oscillation via anomalous Hall effect (AHE) and planar Hall effect (PHE). The first harmonic (fundamental) voltage  $V_{1\omega}$  represents the magnetization direction at equilibrium and the out-of-phase second harmonic voltage  $V_{2\omega}$  provides information on the current-induced effective fields acting on the magnetization. We define  $R_{i\omega} \equiv V_{i\omega}/(I_0/\sqrt{2})$  ( $i = 1, 2$ ) to represent the harmonic signals.

Contributions to  $R_{2\omega}$  include five terms.  $R_{\text{DL}}$ ,  $R_{\text{FL}}$ ,  $R_{\text{Oe}}$ , which reflect changes in  $R_{2\omega}$  caused by  $H_{\text{DL}}$ ,  $H_{\text{FL}}$  and  $H_{\text{Oe}}$ , respectively, decay with increasing  $H_{\text{ext}}$ .  $R_{\text{DL}}$  is proportional to the  $x$  component of the magnetization ( $\cos \varphi$ ) whereas  $R_{\text{FL}} + R_{\text{Oe}}$  scales with  $\cos 2\varphi \cos \varphi$  due to the combined influences of AHE and PHE[40, 41]. Current induced Joule heating and the different thermal conductivity of the substrate and air can lead to an out-of-plane temperature gradient[41] across the heterostructure. With the temperature gradient, the

anomalous Nernst effect (ANE) of CoFeB and the collective action of the spin Seebeck effect (SSE)[60] in CoFeB followed by the inverse spin Hall effect (ISHE) in  $\text{Bi}_{1-x}\text{Sb}_x$  result in a contribution ( $R_{\text{const}}$ ) that does not depend on the size of  $H_{\text{ext}}$ . Applying a field orthogonal to the out-of-plane temperature gradient produces the last term,  $R_{\text{ONE}}$ , due to the ordinary Nernst effect (ONE)[43].  $R_{\text{ONE}}$  scales linearly with  $H_{\text{ext}}$ . The ONE of CoFeB is negligible compared to that of  $\text{Bi}_{1-x}\text{Sb}_x$  due to the difference in the carrier density. Both  $R_{\text{const}}$  and  $R_{\text{ONE}}$  scale with  $\cos \varphi$ .

Putting together these contributions (and assuming  $\varphi \sim \varphi_H$ ),  $R_{2\omega}$  reads:

$$\begin{aligned} R_{2\omega} &= R_{\text{DL}} + R_{\text{ONE}} + R_{\text{const}} + R_{\text{FL}} + R_{\text{Oe}} \\ &= \left( R_{\text{AHE}} \frac{H_{\text{DL}}}{H_{\text{ext}} + H_{\text{K}}} + \frac{\mathcal{N}w\Delta T}{I_0} H_{\text{ext}} + \frac{\alpha w\Delta T}{I_0} \right) \cos \varphi_H \\ &\quad - 2R_{\text{PHE}} \frac{H_{\text{FL}} + H_{\text{Oe}}}{H_{\text{ext}}} \cos 2\varphi_H \cos \varphi_H, \end{aligned} \quad (1)$$

where  $R_{\text{AHE}}$  is the anomalous Hall resistance,  $R_{\text{PHE}}$  is the planar Hall resistance,  $H_{\text{K}}$  is the out-of-plane anisotropy field,  $\mathcal{N}$  is the ONE coefficient of  $\text{Bi}_{1-x}\text{Sb}_x$  and  $\alpha$  is a coefficient that reflects the size of ANE and the combined action of SSE and ISHE. The distinct  $H_{\text{ext}}$  and  $\varphi_H$  dependence of  $R_{2\omega}$  for these contributions allows unambiguous separation of each term from the raw  $R_{2\omega}$  signal. We first decompose  $R_{2\omega}$  into two contributions of different  $\varphi_H$  dependence, *i.e.*  $\cos \varphi_H$  and  $\cos 2\varphi_H \cos \varphi_H$ , and define the prefactors of these two parts as  $A$  and  $B$ , respectively:

$$A \equiv R_{\text{AHE}} \frac{H_{\text{DL}}}{H_{\text{ext}} + H_{\text{K}}} + \frac{V_{\text{ONE}}}{I_0} H_{\text{ext}} + \frac{V_{\text{const}}}{I_0}, \quad (2)$$

$$B \equiv -2R_{\text{PHE}} \frac{H_{\text{FL}} + H_{\text{Oe}}}{H_{\text{ext}}}. \quad (3)$$

Two parameters  $V_{\text{ONE}} \equiv \mathcal{N}w\Delta T$  and  $V_{\text{const}} \equiv \alpha w\Delta T$  are defined to describe the thermoelectric contributions. The  $H_{\text{ext}}$  dependence of  $A$  and  $B$  are then fitted based on Eqs. (2) and (3), respectively.

Representative  $R_{2\omega}$  as a function of  $\varphi_H$  obtained using different  $H_{\text{ext}}$  for 10.9  $\text{Bi}_{0.53}\text{Sb}_{0.47}/2$  CoFeB heterostructure is shown in Fig. 6(a). Solid lines in the figure are fits to the data using Eq. (1). See supplementary materials for the  $\varphi_H$  dependence of  $R_{1\omega}$ . All data shown in this paper are collected using  $\omega/2\pi = 17.5$  Hz. The current amplitude is typically set to  $\sim 1.5$  mA<sub>rms</sub>, which corresponds to a current density in the  $\text{Bi}_{1-x}\text{Sb}_x$  layer of  $\sim 1 \times 10^{10}$  A/m<sup>2</sup>. We find  $R_{2\omega}$  scales linearly with current (data not shown). The  $H_{\text{ext}}$  dependence

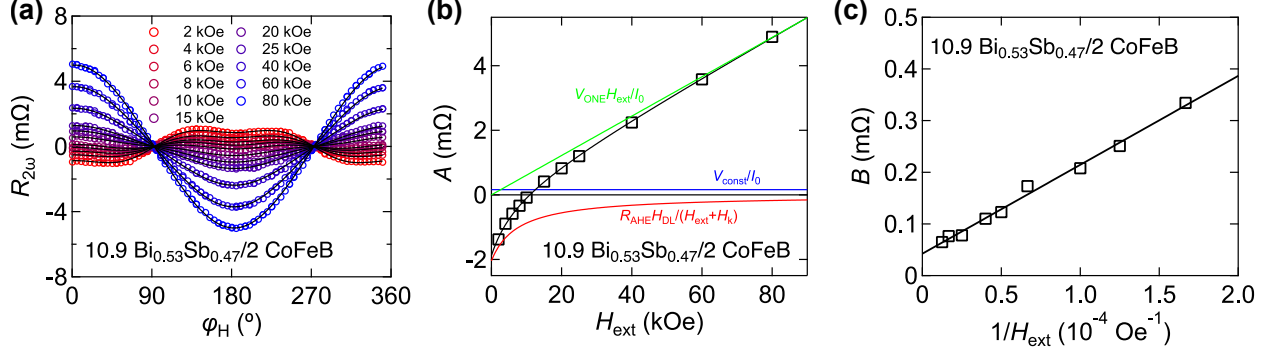


FIG. 6. **Representative second harmonic Hall resistances.** (a) Field angle  $\varphi_H$ -dependence of the second harmonic Hall resistance  $R_{2\omega}$  for  $10.9 \text{ Bi}_{0.53}\text{Sb}_{0.47}/2 \text{ CoFeB}$  heterostructure obtained using different  $H_{\text{ext}}$  measured at 300 K. (b)  $H_{\text{ext}}$  dependence of the fitting parameter  $A$ . (c)  $1/H_{\text{ext}}$  dependence of the fitting parameter  $B$ . In (b) and (c), the colored lines show contributions from each component described in Eqs. (2) and (3): the black solid line show the sum of all contributions.

of one of the fitting parameters  $A$  is shown in Fig. 6(b). The best fit to  $A$  against  $H_{\text{ext}}$  is shown by the solid black line. The colored lines represent decomposition of each contribution following Eq. (2) (see supplementary materials for determination of  $R_{\text{AHE}}$  and  $H_K$ ). In the small  $H_{\text{ext}}$  range,  $R_{\text{DL}}$  term (red line) dominates, whereas at larger field,  $A$  changes sign and is eventually dominated by  $R_{\text{ONE}}$  (green line).  $B$  is plotted against  $1/H_{\text{ext}}$  in Fig. 6(c) with the black solid line showing the best linear fit to the data using Eq. (3). We extract  $H_{\text{DL}}$ ,  $H_{\text{FL}} + H_{\text{Oe}}$ ,  $V_{\text{ONE}}$ , and  $V_{\text{const}}$  from the two fits. We find  $V_{\text{const}}$  and  $V_{\text{ONE}}$  to be proportional to the square of the current flowing within the CoFeB and  $\text{Bi}_{1-x}\text{Sb}_x$  layer, respectively. These results confirm the thermoelectric origin of these contributions and the validity of the interpretation of  $R_{2\omega}$ .

## SUPPLEMENTARY MATERIALS

Supplementary material for this article is available at...

- S1. STEM results of films.
- S2. Magnetic properties of BiSb/CoFeB.
- S3. Anomalous Hall resistance and anisotropy field.

S4. First harmonic Hall resistance of BiSb/CoFeB.

S5. Two-band model analysis of BiSb.

S6. Evaluation of the SOT analysis protocol.

S7. The efficiency of BiSb SOT.

Figure S1. HAADF-STEM and EDS mapping.

Figure S2. Saturation magnetization and magnetic dead layer thickness.

Figure S3. Anomalous Hall resistance and anisotropy field.

Figure S4. First harmonic Hall resistance.

Figure S5. Temperature dependence of magneto-transport properties of  $\text{Bi}_{1-x}\text{Sb}_x$ .

Figure S6. SOT measurements of a standard sample: Pt/CoFeB.

References [61–70].

**Acknowledgements:** We thank Y. Fuseya, H. Kohno, G. Qu for helpful discussions.

**Fundings:** This work was partly supported by JSPS Grant-in-Aid for Scientific Research (Grant No. 16H03853), Specially Promoted Research (Grant No. 15H05702), Casio Science Foundation, and the Center for Spintronics Research Network (CSRN). Z.C. acknowledges financial support from Materials Education program for the future leaders in Research, Industry, and Technology (MERIT). Y.-C.L. is supported by JSPS International Fellowship for Research in Japan (Grant No. JP17F17064). **Author Contributions:** Y.-C.L., Z.C. M.H. planned the study. Z.C. and Y.-C.L. grew the samples, designed the experimental set-up, performed electrical measurements and carried out data analysis. Y.-C.L. performed structural characterization (AFM, XRD), fabricated Hall bar devices, and modeled the system transport properties. X.-D.X., T.O. and K.H. carried out TEM imaging. Z.C. and Y.-C.L. wrote the manuscript with input from M.H. All authors contributed to the discussion of results and commented on the manuscript. **Competing interests:** The authors declare no competing interests. **Data and materials availability:** All data needed to evaluate the conclusions in the paper are present in the paper and/or the supplementary materials. Additional data related to this paper may be requested from the corresponding authors.

## S1. STEM results of films

We performed high-angle annular dark-field scanning transmission electron microscopy (HAADF-STEM) analysis of samples using a FEI Titan<sup>TM</sup> G2 80-200 transmission electron microscope with a probe forming aberration corrector operated at 200 kV. Samples were cross-sectioned into thin lamellae by focused ion beam (FIB) lift-out technique using FEI Helios G4 UX. Nanobeam electron diffraction patterns were taken with a 10- $\mu\text{m}$ -diameter condenser aperture. Element-selected analysis were carried out via energy-dispersive X-ray spectroscopy (EDS)[61].

Figure S1(a) shows a HAADF-STEM image and the corresponding EDS maps of one of the heterostructures with 10.9 Bi<sub>0.53</sub>Sb<sub>0.47</sub>/2 CoFeB. EDS line scans averaged over the entire image ( $19 \times 26 \text{ nm}^2$ ) are shown in Fig. S1(b). We find that Sb tends to diffuse toward the CoFeB layer. This may be attributed to the finite solubility of Sb in Co and Fe, in contrast to Bi which is practically immiscible with any of these elements.

## S2. Magnetic properties of BiSb/CoFeB

Magnetic moments of the heterostructures were measured using a vibrating sample magnetometer (VSM) at room temperature. A superconducting quantum interference device (SQUID) is used to measure the temperature dependence of the magnetic properties. The magnetization hysteresis loops of a heterostructure with 5.6 Bi<sub>0.53</sub>Sb<sub>0.47</sub>/2 CoFeB are displayed in Fig. S2(a) under an external magnetic field applied parallel and perpendicular to film plane. The magnetic easy axis of the CoFeB layer points along the film plane.

The  $t_{\text{CoFeB}}$  dependence of the saturated magnetic moment of heterostructures with two different Bi<sub>0.53</sub>Sb<sub>0.47</sub> layer thicknesses are plotted in Fig. S2(b). Data from the two series are hardly discernable. We therefore assume that the saturation magnetization  $M_s$  and the magnetic dead layer thickness  $t_D$  of the CoFeB layer are independent of the Bi<sub>1-x</sub>Sb<sub>x</sub> thickness. Linear fit to all the data are shown in Fig. S2(b) as the solid line. From the slope and the  $x$ -intercept of the linear line,  $M_s$  and  $t_D$  are determined to be  $1190 \pm 20 \text{ emu/cm}^3$  and  $0.46 \pm 0.04 \text{ nm}$ , respectively. In Fig. S2(b), we also show  $M_s$  values of heterostructures with 10 Bi/2 CoFeB and 10 Sb/2 CoFeB. As we find almost no difference in  $M_s$  when the Sb concentration is changed, we assume a constant  $M_s$  and  $t_D$  for all heterostructures studied (with different  $x$ ).

Figure S2(c) shows the magnetization hysteresis loops of the same heterostructure shown in (a) evaluated at 300 K and 10 K. A SQUID magnetometer is used: the field is applied along the film plane. The two loops measured at 300 K and 10 K overlap. We thus assume the temperature has little influence on  $M_s$  of CoFeB for all samples.

### S3. Anomalous Hall resistance and anisotropy field

The Hall resistance  $R_{xy}$  of the heterostructures are measured using a dc current of 20  $\mu\text{A}$ . An exemplary loop of  $R_{xy}$  vs.  $H_z$  is displayed in Fig. S3(a). The slope of  $R_{xy}$  at large magnetic field is attributed to the ordinary Hall effect of BiSb. Data at large magnetic field is fitted using a linear function. The anomalous Hall resistance  $R_{\text{AHE}}$  is obtained from the  $y$ -axis intercept of the fitted linear function shown by the red dotted lines[42]. The low field data are also fitted with a linear function, as shown by the blue dotted line. The out-of-plane anisotropy field  $H_K$  is determined by the  $x$ -intercept of the two linear functions: see Fig. S3(a) for an illustration to obtain  $H_K$  from the loop.

Figure S3(b) and (e) show the layer thickness dependence of  $R_{\text{AHE}}$  and  $H_K$ , respectively. As evident,  $|R_{\text{AHE}}|$  decreases with increasing  $\text{Bi}_{1-x}\text{Sb}_x$  thickness regardless of the size of  $t_{\text{CoFeB}}$  (Fig. S3(b)), which is attributed to current shunting into the  $\text{Bi}_{1-x}\text{Sb}_x$  layer. Figure S3(e) shows that  $H_K$  is nearly independent of the  $\text{Bi}_{1-x}\text{Sb}_x$  layer thickness.  $H_K$  increases with decreasing CoFeB layer thickness, which is consistent with the presence of a perpendicular magnetic anisotropy at the CoFeB/MgO interface[62]. The Sb concentration ( $x$ ) dependence of  $R_{\text{AHE}}$  and  $H_K$  are displayed in Fig. S3(c) and S3(f), respectively. We find  $|R_{\text{AHE}}|$  decreases with increasing Sb concentration, which is predominantly due to larger current shunting into the  $\text{Bi}_{1-x}\text{Sb}_x$  layer as the layer conductivity increases with increasing  $x$  (see Fig. 3(a)).  $H_K$  tends to increase with increasing  $x$ . Although the underlying mechanism is not clear, these results indicate that the perpendicular magnetic anisotropy, predominantly defined at the CoFeB/MgO interface, is influenced by the underlayer[63]. The temperature dependence of  $R_{\text{AHE}}$  and  $H_K$  for heterostructures with 10  $\text{Bi}_{1-x}\text{Sb}_x/2$  CoFeB are shown in Fig. S3(d) and (g), respectively. For all  $x$  studied, both  $|R_{\text{AHE}}|$  and  $H_K$  tend to increase with decreasing temperature. Changes in  $R_{\text{AHE}}$  are mainly attributed to the different temperature dependence of the conductivity of  $\text{Bi}_{1-x}\text{Sb}_x$  and CoFeB. Whereas the conductivity of CoFeB is practically independent of the temperature, that of  $\text{Bi}_{1-x}\text{Sb}_x$  de-

creases with decreasing temperature, resulting in redistribution of the current within the two layers on varying the temperature. The increase of  $H_K$  with temperature is unclear and requires further investigation.

#### S4. First harmonic Hall resistance of BiSb/CoFeB

Exemplary results of the first harmonic Hall resistance  $R_{1\omega}$  plotted against the angle  $\varphi_H$  (the angle between the external magnetic field applied along the film plane and the  $x$  axis) are shown in Fig. S4(a). The results can be fitted using the following function:

$$R_{1\omega} = R_{\text{PHE}} \sin 2\varphi_H + \zeta R_{\text{AHE}} \cos \varphi_H, \quad (\text{S4})$$

where  $\zeta$  is a constant that is introduced to take into account an unintentional misalignment between the external magnetic field and the film plane. We use Eq. (S4) to obtain the planar Hall resistance  $R_{\text{PHE}}$ . We find little change in  $R_{1\omega}$  on varying the magnetic field, suggesting good sample alignment and weak external field dependence of  $R_{\text{PHE}}$ . We therefore take the average  $R_{\text{PHE}}$  obtained under different magnetic fields.

Figure S4(b) illustrates the  $\text{Bi}_{1-x}\text{Sb}_x$  and CoFeB layer thickness dependence of  $R_{\text{PHE}}$ . Note that in heavy metal/CoFeB bilayers  $R_{\text{PHE}}$  contains contribution from the spin Hall magnetoresistance (SMR)[64, 65]. We find a peak in  $|R_{\text{PHE}}|$  at  $t_{\text{BiSb}} \sim 5$  nm, which is approximately twice of the  $\text{Bi}_{1-x}\text{Sb}_x$  spin diffusion length ( $\sim 2.3$  nm) determined in the main text. The position of the peak in  $|R_{\text{PHE}}|$  is consistent with the SMR theory[18].  $R_{\text{PHE}}$  for heterostructures with  $10 \text{ Bi}_{1-x}\text{Sb}_x/2 \text{ CoFeB}$  are plotted as a function of Sb concentration ( $x$ ) and temperature in Fig. S4(c) and S4(d) respectively. We consider these changes are mainly due to variation of the spin Hall efficiency and current redistribution within the bilayers.

#### S5. Two-band model analysis of BiSb

Carrier concentration and mobility of  $\text{Bi}_{1-x}\text{Sb}_x$  are estimated based on a classical two-carrier model, *i.e.* both electrons and holes contribute to the transport. Experimental inputs of the model are: Hall coefficient  $R_H$  (given by  $R_H = R_{xy}t_{\text{BiSb}}/H_z$ , where  $H_z$  represents  $H_{\text{ext}}$  along the  $z$ -axis), longitudinal conductivity at zero field  $\sigma_{\text{BiSb}}$  and the quadratic component

of the transverse magnetoresistance (MR) with  $H_z$ . The equations read[66]:

$$R_H = \frac{(n_e \mu_e^2 - n_h \mu_h^2) + (n_h - n_e) \mu_h^2 \mu_e^2 H_z^2}{e (n_h \mu_h + n_e \mu_e)^2 + (n_h - n_e)^2 \mu_h^2 \mu_e^2 H_z^2}, \quad (\text{S5})$$

$$\sigma_{\text{BiSb}} = e (n_h \mu_h + n_e \mu_e), \quad (\text{S6})$$

$$\text{MR} = \frac{\rho_{\text{BiSb}}(H_z) - \rho_{\text{BiSb}}(H_z = 0)}{\rho_{\text{BiSb}}(H_z = 0)} = \frac{n_h \mu_h n_h \mu_h (\mu_h + \mu_e)^2 H_z^2}{(n_h \mu_h + n_e \mu_e)^2 + (n_h - n_e)^2 (\mu_h \mu_e)^2 H_z^2}. \quad (\text{S7})$$

Here,  $n_h(n_e)$  and  $\mu_h(\mu_e)$  denote the carrier density and the mobility of hole(electron), respectively. Since Bi and Sb have the same number of  $p$  valence electrons, we assume  $n_h \approx n_e \equiv n$  for all  $x$  of  $\text{Bi}_{1-x}\text{Sb}_x$ . With such carrier compensation, Eqs. (S5), (S5) and (S5) can be reduced to:

$$R_H = \frac{ne(\mu_e^2 - \mu_h^2)}{\sigma_{\text{BiSb}}^2}, \quad (\text{S8})$$

$$\sigma_{\text{BiSb}} = ne(\mu_h + \mu_e), \quad (\text{S9})$$

$$\text{MR} = \mu_e \mu_h H_z^2 = \beta H_z^2. \quad (\text{S10})$$

Based on these equations,  $n$  and mobilities  $\mu_h, \mu_e$  can be estimated from experimental results. As an example, the temperature dependences of  $R_{xy}$  and MR for 10  $\text{Bi}_{0.83}\text{Sb}_{0.17}$  grown on Ta seed layer are shown in Fig. S5(a) and S5(b).  $R_H$  and  $\beta \equiv \mu_e \mu_h$  extracted from the plots are shown in Fig. S5(c) and S5(d), respectively. The large quasi-linear MR at 10 K is mainly attributed to the weak anti-localization of  $\text{Bi}_{1-x}\text{Sb}_x$  exhibiting strong spin orbit coupling. We therefore limit our analysis of carrier density and mobility to temperature ranging from 50 K to 300 K. The estimated  $n, \mu_h$  and  $\mu_e$  are shown in Fig. 5 of the manuscript.

## S6. Evaluation of the SOT analysis protocol

To verify the analysis protocol used here, the damping-like and field-like SOTs for a standard sample, Sub./1 Ta/3.3 Pt/2 CoFeB/2 MgO/1 Ta (thicknesses in nm) heterostructure, was measured. Figure S6(a) shows the resistivity of Pt ( $\rho_{\text{Pt}}$ ) as a function of temperature. A parallel circuit model is employed to estimate the resistivity of Pt; we assume the only other conducting layer is CoFeB, which has a resistivity of  $\rho_{\text{CoFeB}} \sim 140 \mu\Omega\text{cm}$ . We find  $\rho_{\text{Pt}}$  is  $\sim 44 \mu\Omega\text{cm}$  at room temperature and decreases to  $\sim 38 \mu\Omega\text{cm}$  at 5 K, reflecting the metallic transport property of Pt (the small residual-resistance ratio indicates large amount of impurity in Pt). Parameter  $A$  at 300K, which is defined in Eq. (2) of the main text, is plotted as a function of  $H_{\text{ext}}$  in Fig. S6(b). The colored lines represent contributions from

different components. Thermoelectric signals in Pt/CoFeB are sufficiently small compared to the signal due to SOT. Figure S6(c) shows the damping-like spin Hall efficiency  $\xi_{\text{DL}}$  and the spin Hall conductivity  $\sigma_{\text{SH}}$  plotted as a function of temperature. We find  $\xi_{\text{DL}} \sim 0.06$  at room temperature, corresponding to  $\sigma_{\text{SH}} \sim 650 (\hbar/e)\Omega^{-1}\text{cm}^{-1}$ .  $\xi_{\text{DL}}$  and  $\sigma_{\text{SH}}$  slightly increase with increasing temperature, consistent with previous results obtained in similar heterostructures (Pt/Py) evaluated using the spin-torque ferromagnetic resonance (ST-FMR) technique[67] and lateral spin valve measurements[58].

## S7. The efficiency of BiSb SOT

Although BiSb exhibit a large spin Hall efficiency, its resistivity is larger than typical metals, including the ferromagnetic metals that are used when forming SOT devices. Here we estimate the critical current needed to control the magnetization direction of the adjacent ferromagnet using BiSb and compare it with other materials. We consider a bilayer composed of a ferromagnetic metal (FM) layer and a non-magnetic metal (NM) layer, i.e. the latter generates spin current via the spin Hall effect. The critical current density is defined as the NM layer charge current density  $j_{\text{NM}}$  required to generate sufficient damping-like SOT to induce switching of the FM layer magnetization. In the macrospin limit,  $j_{\text{NM}}$  takes the form[68]:

$$j_{\text{NM}} = \frac{eH_{\text{K,eff}}M_s t_{\text{FM}}}{2\hbar\xi_{\text{DL}}} f(h_x), \quad (\text{S11})$$

where  $H_{\text{K,eff}}$  is the effective anisotropy field,  $M_s$  is the saturation magnetization of the FM layer, and  $f(h_x)$  is a function of  $h_x \equiv \frac{H_x}{H_{\text{K,eff}}}$ .  $H_x$  is the external in-plane field  $H_x$ ,  $e$  and  $\hbar$  are the electric charge and the reduced Planck constant, respectively. Here we have assumed a perpendicularly magnetized system to estimate the switching current; however, the only factor that is relevant in the following discussion is the spin Hall efficiency  $\xi_{\text{DL}}$ . For simplicity, we assume the properties of the FM layer do not depend on the NM layer. The resistivity of the NM and FM layers are defined as  $\rho_{\text{NM}}$  and  $\rho_{\text{FM}}$ , respectively. Assuming a parallel circuit, the overall current that flows in the bilayer when  $j_{\text{NM}}$  is applied to the NM layer is given as

$$I_c = j_{\text{NM}} w \frac{\rho_{\text{NM}} t_{\text{FM}} + \rho_{\text{FM}} d_{\text{NM}}}{\rho_{\text{FM}}}, \quad (\text{S12})$$

where  $w$  is the width of the device, which we assume is the same for both NM and FM layers. To compare the efficiency of BiSb with other materials system, we substitute typical values

of the relevant parameters and estimate  $I_c$ . We compare BiSb/CoFeB with W/CoFeB[69], the latter being the prototype of SOT-MRAM[70]. The parameters assumed are:  $t_{\text{CoFeB}} = 1$  nm and  $\rho_{\text{CoFeB}} = 150 \mu\Omega\text{cm}$  for FM=CoFeB,  $d_{\text{W}} = 5$  nm,  $\rho_{\text{W}} = 120 \mu\Omega\text{cm}$ ,  $\xi_{\text{DL,W}}=0.3$  for NM=W, and  $d_{\text{BiSb}} = 10$  nm,  $\rho_{\text{BiSb}} = 1000 \mu\Omega\text{cm}$ ,  $\xi_{\text{DL,BiSb}}=1.2$  for NM=BiSb. The ratio of the critical current becomes

$$\frac{I_{c,W}}{I_{c,\text{BiSb}}} = \frac{\xi_{\text{DL,BiSb}}}{\xi_{\text{DL,W}}} \frac{\rho_{\text{W}} t_{\text{CoFeB}} + \rho_{\text{CoFeB}} d_{\text{W}}}{\rho_{\text{BiSb}} t_{\text{CoFeB}} + \rho_{\text{CoFeB}} d_{\text{BiSb}}} \sim 1.4. \quad (\text{S13})$$

Thus we find the large spin Hall efficiency of BiSb is beneficial for SOT-MRAM even for its large resistivity: the current can be reduced by  $\sim 40\%$  compared to the state of art materials system, W/CoFeB.

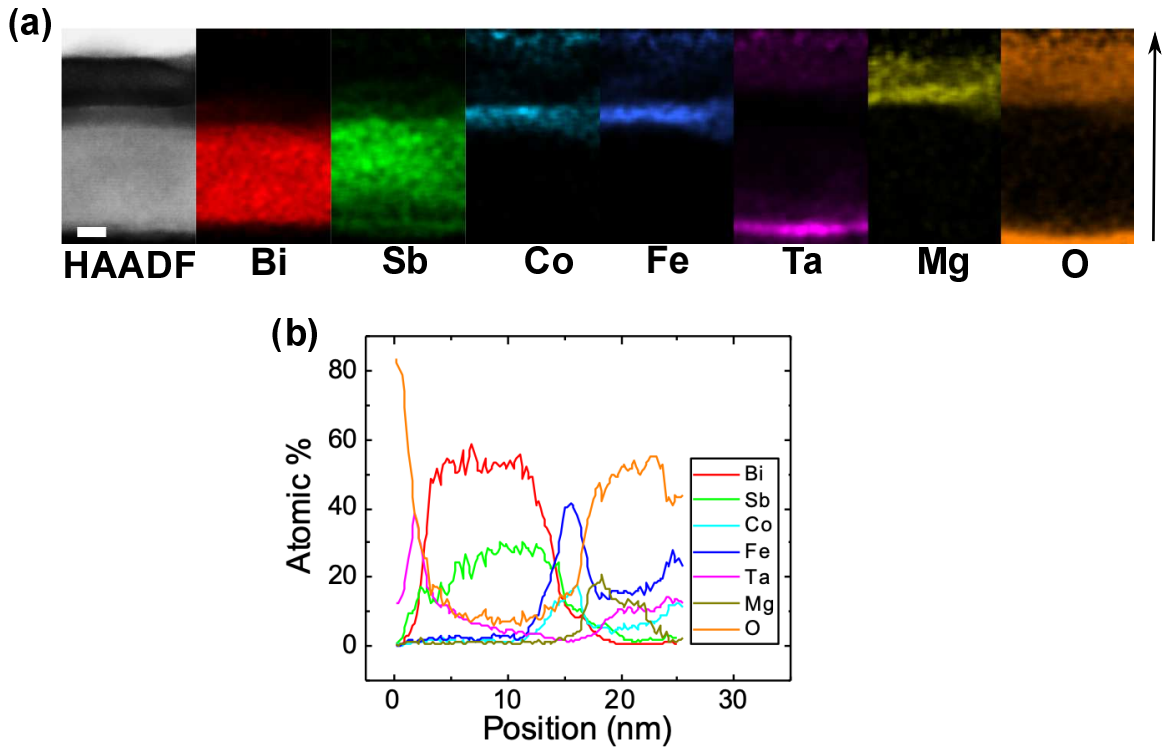


FIG. S1. **HAADF-STEM and EDS mapping.** (a) HAADF-STEM and elemental EDS maps of a heterostructure with  $10.9 \text{ Bi}_{0.53}\text{Sb}_{0.47}/2 \text{ CoFeB}$ . The length of the horizontal white bar corresponds to  $\sim 2$  nm in the image. (b) Position dependence of the atomic ratio for different elements. The black arrow in (a) indicates the direction of the line scans. Position zero corresponds to the substrate/heterostructure interface.

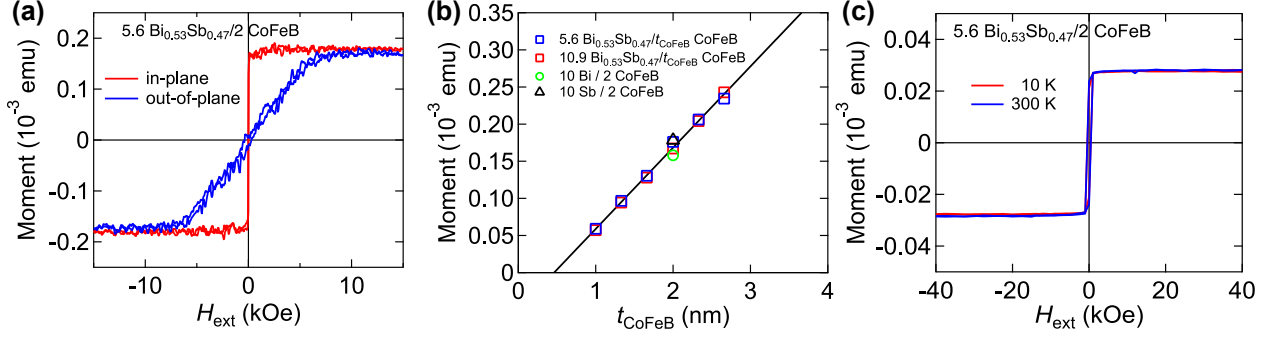


FIG. S2. **Saturation magnetization and magnetic dead layer thickness.** (a) Magnetization hysteresis loops of a heterostructure with 5.6 Bi<sub>0.53</sub>Sb<sub>0.47</sub>/2 CoFeB. The red and blue lines show the hysteresis when the field is applied along and normal to the film plane, respectively. (b) CoFeB thickness dependence of the saturated magnetic moment for heterostructures with 5.6 Bi<sub>0.53</sub>Sb<sub>0.47</sub>/t<sub>CoFeB</sub> CoFeB (blue squares) and 10.9 Bi<sub>0.53</sub>Sb<sub>0.47</sub>/t<sub>CoFeB</sub> CoFeB (red squares). The solid line represents linear fit to the data. The slope and the  $x$ -axis intercept of the linear line allows one to determine the saturation magnetization and the magnetic dead layer thickness, respectively. Data from heterostructures with 10 Bi/2 CoFeB and 10 Sb/2 CoFeB are laid together using green circle and black triangle, respectively. (c) In-plane magnetization hysteresis loops of a heterostructure with 5.6 Bi<sub>0.53</sub>Sb<sub>0.47</sub>/2 CoFeB. The red and blue lines represent hysteresis loops obtained at measurement temperatures of 10 K and 300 K, respectively. The results shown in (a) and (b) are obtained using VSM: the specimen film area is  $\sim 9.6 \times 9.6$  mm<sup>2</sup>. SQUID is used to obtain the results shown in (c): the specimen film area is roughly  $2 \times 6$  mm<sup>2</sup>.

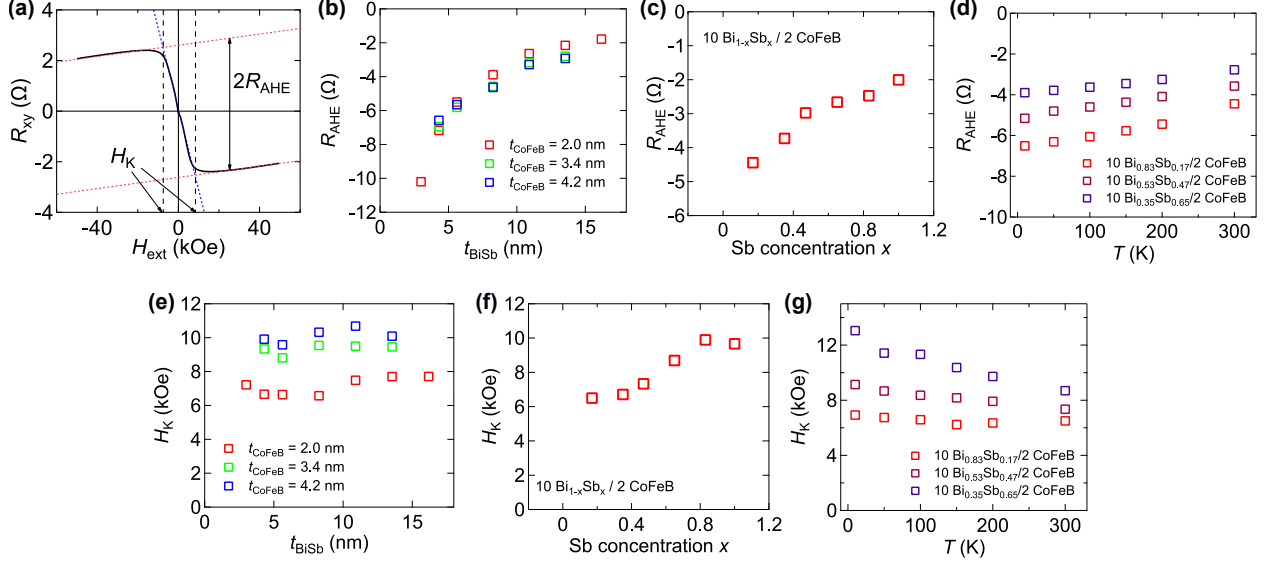


FIG. S3. **Anomalous Hall resistance and anisotropy field.** (a) Hall resistance  $R_{xy}$  of a heterostructure with  $10.9 \text{ Bi}_{0.53}\text{Sb}_{0.47}/2 \text{ CoFeB}$  plotted as a function of magnetic field  $H_{ext}$  along the film normal (along the  $z$ -axis). Red and blue dashed lines show linear fits to the data in the high-field and low-field ranges, respectively. Definitions of the anomalous Hall resistance  $R_{AHE}$  and the anisotropy field  $H_K$  are illustrated in the panel. (b-g)  $R_{AHE}$  and  $H_K$  of heterostructures with  $t_{\text{BiSb}} \text{ Bi}_{1-x}\text{Sb}_x/t_{\text{CoFeB}} \text{ CoFeB}$  plotted as a function of  $\text{Bi}_{1-x}\text{Sb}_x$  thickness  $t_{\text{BiSb}}$  (b,e), Sb concentration  $x$  (c,f) and the measurement temperature  $T$  (d,g).

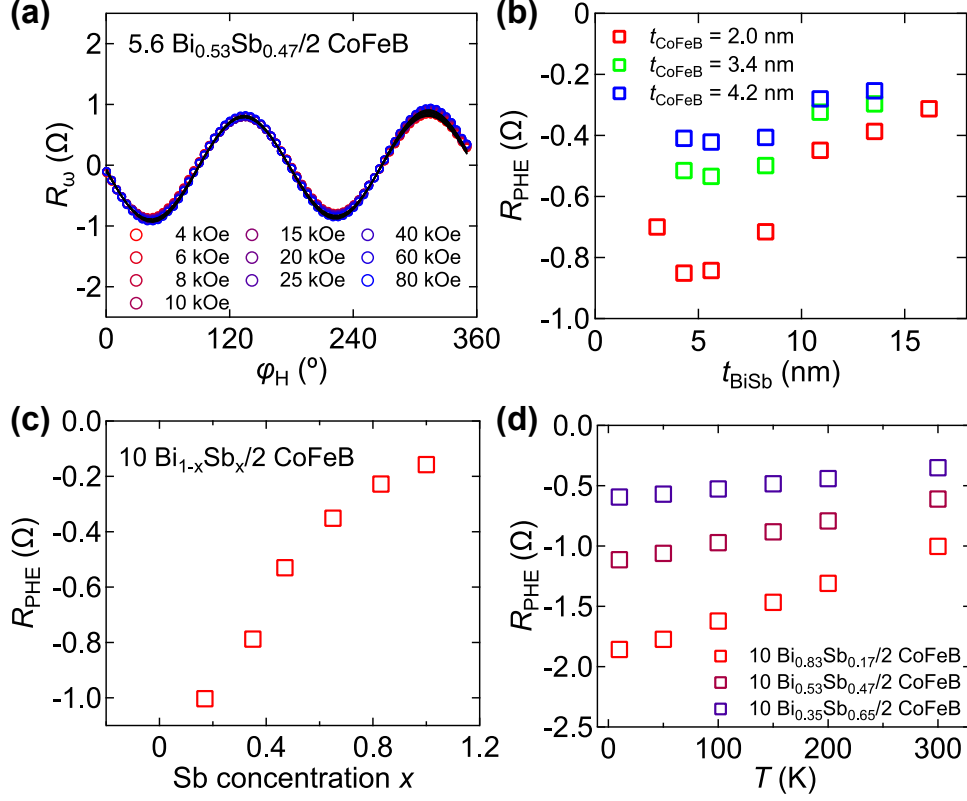


FIG. S4. **First harmonic Hall resistance.** (a) Field angle  $\varphi_H$  dependence of the first harmonic Hall resistance  $R_{1\omega}$  of a heterostructure with 5.6 Bi<sub>0.53</sub>Sb<sub>0.47</sub>/2 CoFeB. Different symbols represent results obtained from various strengths of in-plane magnetic field. The black lines show the fitting with Eq. (S4). (b-d) Planar Hall resistance  $R_{\text{PHE}}$  plotted against Bi<sub>1-x</sub>Sb<sub>x</sub> thickness  $t_{\text{BiSb}}$  (b), Sb concentration  $x$  (c) and the measurement temperature  $T$  (d), respectively.

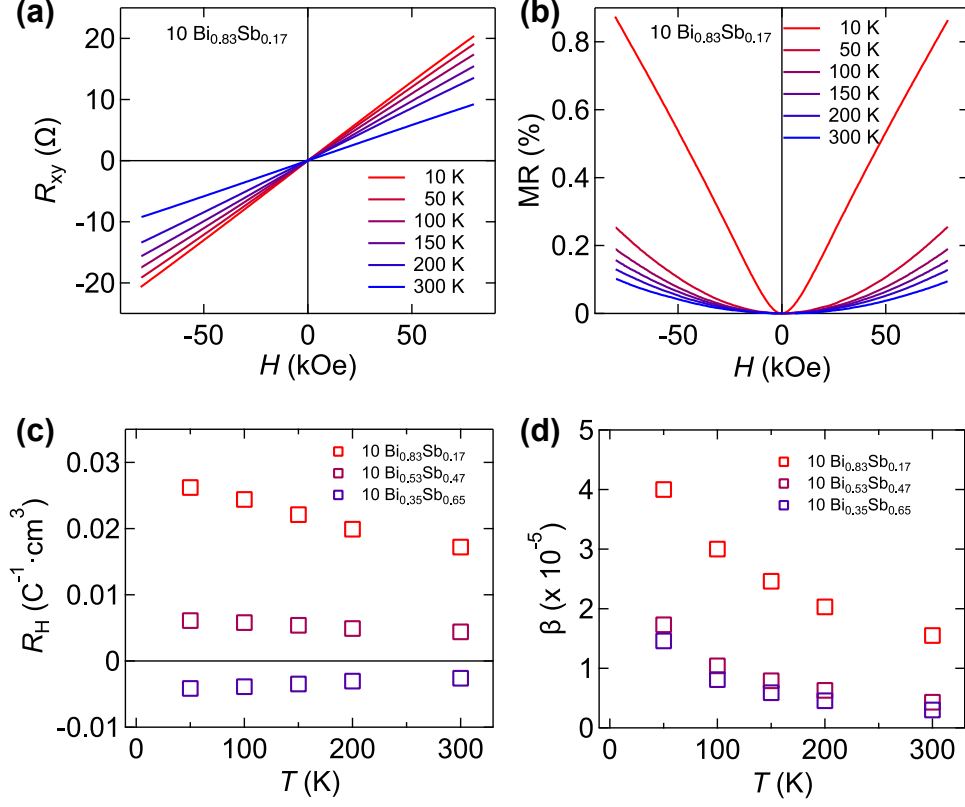


FIG. S5. **Temperature dependence of magneto-transport properties of  $\text{Bi}_{1-x}\text{Sb}_x$ .** (a-b) Temperature dependence of  $R_{xy}$  (a) and the magnetoresistance (MR) (b) plotted against external field  $H_{\text{ext}}$  along  $z$  for a heterostructure with 10  $\text{Bi}_{0.83}\text{Sb}_{0.17}$  (without the CoFeB layer). (c,d) Hall coefficient  $R_H$  (c) and MR coefficient  $\beta$  (d) for  $\text{Bi}_{1-x}\text{Sb}_x$  heterostructures (without the CoFeB layer) of different compositions plotted as a function of temperature.

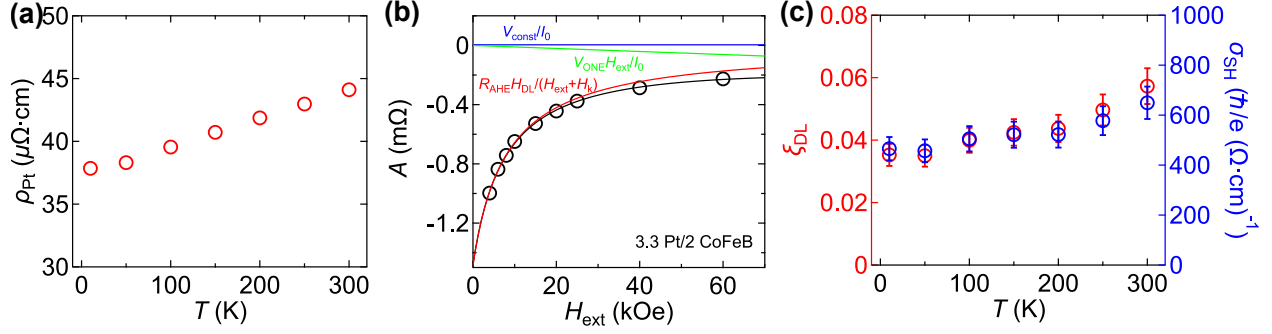


FIG. S6. **SOT measurements of a standard sample: Pt/CoFeB.** (a-c) The film structure is Sub./1 Ta/3.3 Pt/2 CoFeB/2 MgO/1 Ta (thicknesses in nm). (a) Temperature dependence of the Pt layer resistivity  $\rho_{\text{Pt}}$ . (b)  $H_{\text{ext}}$  dependence of fitting parameter  $A$  obtained at measurements carried out at room temperature. (c) Temperature dependence of the damping-like spin Hall efficiency  $\xi_{\text{DL}}$  and the spin Hall conductivity  $\sigma_{\text{SH}}$ .

- 
- [1] S. Murakami, N. Nagaosa, and S. C. Zhang, “Dissipationless quantum spin current at room temperature,” *Science* **301**, 1348–1351 (2003).
- [2] W. L. Lee, S. Watauchi, V. L. Miller, R. J. Cava, and N. P. Ong, “Dissipationless anomalous hall current in the ferromagnetic spinel  $\text{CuCr}_2\text{Se}_4$ ,” *Science* **303**, 1647–1649 (2004).
- [3] M. I. Dyakonov and V. I. Perel, “Possibility of orienting electron spins with current,” *Jetp Letters-Ussr* **13**, 467 (1971).
- [4] J. E. Hirsch, “Spin hall effect,” *Phys. Rev. Lett.* **83**, 1834–1837 (1999).
- [5] Jairo Sinova, Sergio O. Valenzuela, J. Wunderlich, C. H. Back, and T. Jungwirth, “Spin hall effects,” *Rev. Mod. Phys.* **87**, 1213–1259 (2015).
- [6] Y. A. Bychkov and E. I. Rashba, “Properties of a 2d electron-gas with lifted spectral degeneracy,” *Jetp Lett.* **39**, 78–81 (1984).
- [7] V. M. Edelstein, “Spin polarization of conduction electrons induced by electric-current in 2-dimensional asymmetric electron-systems,” *Solid State Communications* **73**, 233–235 (1990).
- [8] A. Manchon, H. C. Koo, J. Nitta, S. M. Frolov, and R. A. Duine, “New perspectives for rashba spin-orbit coupling,” *Nat. Mater.* **14**, 871–882 (2015).
- [9] Luqiao Liu, Chi-Feng Pai, Y. Li, H. W. Tseng, D. C. Ralph, and R. A. Buhrman, “Spin-torque switching with the giant spin hall effect of tantalum,” *Science* **336**, 555–558 (2012).
- [10] I. M. Miron, G. Gaudin, S. Auffret, B. Rodmacq, A. Schuhl, S. Pizzini, J. Vogel, and P. Gambardella, “Current-driven spin torque induced by the Rashba effect in a ferromagnetic metal layer,” *Nature Materials* **9**, 230–234 (2010).

- [11] J. Kim, J. Sinha, M. Hayashi, M. Yamanouchi, S. Fukami, T. Suzuki, S. Mitani, and H. Ohno, “Layer thickness dependence of the current induced effective field vector in Ta|CoFeB|MgO,” *Nat. Mater.* **12**, 240 (2013).
- [12] K. Garello, I. M. Miron, C. O. Avci, F. Freimuth, Y. Mokrousov, S. Blugel, S. Auffret, O. Boulle, G. Gaudin, and P. Gambardella, “Symmetry and magnitude of spin-orbit torques in ferromagnetic heterostructures,” *Nat. Nanotechnol.* **8**, 587–593 (2013).
- [13] I. M. Miron, K. Garello, G. Gaudin, P. J. Zermatten, M. V. Costache, S. Auffret, S. Bandiera, B. Rodmacq, A. Schuhl, and P. Gambardella, “Perpendicular switching of a single ferromagnetic layer induced by in-plane current injection,” *Nature* **476**, 189–193 (2011).
- [14] Satoru Emori, Uwe Bauer, Sung-Min Ahn, Eduardo Martinez, and Geoffrey S. D. Beach, “Current-driven dynamics of chiral ferromagnetic domain walls,” *Nat. Mater.* **12**, 611–616 (2013).
- [15] Kwang-Su Ryu, Luc Thomas, See-Hun Yang, and Stuart Parkin, “Chiral spin torque at magnetic domain walls,” *Nat. Nanotechnol.* **8**, 527 (2013).
- [16] Seonghoon Woo, Kai Litzius, Benjamin Kruger, Mi-Young Im, Lucas Caretta, Kornel Richter, Maxwell Mann, Andrea Krone, Robert M. Reeve, Markus Weigand, Parnika Agrawal, Ivan Lemes, Mohamad-Assaad Mawass, Peter Fischer, Mathias Klau, and Geoffrey S. D. Beach, “Observation of room-temperature magnetic skyrmions and their current-driven dynamics in ultrathin metallic ferromagnets,” *Nature Materials* **15**, 501–506 (2016).
- [17] H. Nakayama, M. Althammer, Y. T. Chen, K. Uchida, Y. Kajiwara, D. Kikuchi, T. Ohtani, S. Geprags, M. Opel, S. Takahashi, R. Gross, G. E. W. Bauer, S. T. B. Goennenwein, and E. Saitoh, “Spin hall magnetoresistance induced by a nonequilibrium proximity effect,” *Phys. Rev. Lett.* **110**, 206601 (2013).

- [18] Y. T. Chen, S. Takahashi, H. Nakayama, M. Althammer, S. T. B. Goennenwein, E. Saitoh, and G. E. W. Bauer, “Theory of spin hall magnetoresistance,” *Phys. Rev. B* **87**, 144411 (2013).
- [19] J. C. Rojas-Sanchez, N. Reyren, P. Laczkowski, W. Savero, J. P. Attane, C. Deranlot, M. Jamet, J. M. George, L. Vila, and H. Jaffres, “Spin pumping and inverse spin Hall effect in platinum: The essential role of spin-memory loss at metallic interfaces,” *Physical Review Letters* **112**, 106602 (2014).
- [20] Weifeng Zhang, Wei Han, Xin Jiang, See-Hun Yang, and Stuart S. P. Parkin, “Role of transparency of platinum-ferromagnet interfaces in determining the intrinsic magnitude of the spin Hall effect,” *Nature Physics* **11**, 496–502 (2015).
- [21] M. Z. Hasan and C. L. Kane, “Colloquium: Topological insulators,” *Reviews of Modern Physics* **82**, 3045–3067 (2010).
- [22] Yan Sun, Yang Zhang, Claudia Felser, and Binghai Yan, “Strong intrinsic spin Hall effect in the TaAs family of Weyl semimetals,” *Physical Review Letters* **117**, 146403 (2016).
- [23] A. R. Melnik, J. S. Lee, A. Richardella, J. L. Grab, P. J. Mintun, M. H. Fischer, A. Vaezi, A. Manchon, E. A. Kim, N. Samarth, and D. C. Ralph, “Spin-transfer torque generated by a topological insulator,” *Nature* **511**, 449 (2014).
- [24] Y. B. Fan, P. Upadhyaya, X. F. Kou, M. R. Lang, S. Takei, Z. X. Wang, J. S. Tang, L. He, L. T. Chang, M. Montazeri, G. Q. Yu, W. J. Jiang, T. X. Nie, R. N. Schwartz, Y. Tserkovnyak, and K. L. Wang, “Magnetization switching through giant spin-orbit torque in a magnetically doped topological insulator heterostructure,” *Nat. Mater.* **13**, 699–704 (2014).
- [25] M. Jamali, J. S. Lee, J. S. Jeong, F. Mahfouzi, Y. Lv, Z. Y. Zhao, B. K. Nikolic, K. A. Mkhoyan, N. Samarth, and J. P. Wang, “Giant spin pumping and inverse spin hall effect in the presence of surface and bulk spin-orbit coupling of topological insulator  $\text{Bi}_2\text{Se}_3$ ,” *Nano*

- Lett. **15**, 7126–7132 (2015).
- [26] K. Kondou, R. Yoshimi, A. Tsukazaki, Y. Fukuma, J. Matsuno, K. S. Takahashi, M. Kawasaki, Y. Tokura, and Y. Otani, “Fermi-level-dependent charge-to-spin current conversion by dirac surface states of topological insulators,” *Nat. Phys.* **12**, 1027 (2016).
- [27] K. Yasuda, A. Tsukazaki, R. Yoshimi, K. Kondou, K. S. Takahashi, Y. Otani, M. Kawasaki, and Y. Tokura, “Current-nonlinear hall effect and spin-orbit torque magnetization switching in a magnetic topological insulator,” *Phys. Rev. Lett.* **119**, 137204 (2017).
- [28] Y. Wang, D. P. Zhu, Y. Wu, Y. M. Yang, J. W. Yu, R. Ramaswamy, R. Mishra, S. Y. Shi, M. Elyasi, K. L. Teo, Y. H. Wu, and H. Yang, “Room temperature magnetization switching in topological insulator-ferromagnet heterostructures by spin-orbit torques,” *Nat. Commun.* **8**, 1364 (2017).
- [29] J. H. Han, A. Richardella, S. A. Siddiqui, J. Finley, N. Samarth, and L. Q. Liu, “Room-temperature spin-orbit torque switching induced by a topological insulator,” *Phys. Rev. Lett.* **119**, 077702 (2017).
- [30] D. C. Mahendra, R. Grassi, J. Y. Chen, M. Jamali, D. R. Hickey, D. L. Zhang, Z. Y. Zhao, H. S. Li, P. Quarterman, Y. Lv, M. Li, A. Manchon, K. A. Mkhoyan, T. Low, and J. P. Wang, “Room-temperature high spin-orbit torque due to quantum confinement in sputtered  $\text{Bi}_{1-x}\text{Sb}_x$  films,” *Nat. Mater.* **17**, 800 (2018).
- [31] N. H. D. Khang, Y. Ueda, and P. N. Hai, “A conductive topological insulator with large spin hall effect for ultralow power spin-orbit torque switching,” *Nat. Mater.* **17**, 808 (2018).
- [32] Y. F. Li, Q. L. Ma, S. X. Huang, and C. L. Chien, “Thin films of topological kondo insulator candidate  $\text{Sb}_2\text{Te}_3$ : Strong spin-orbit torque without exclusive surface conduction,” *Science Advances* **4**, eaap8294 (2018).

- [33] Y. Liu and R. E. Allen, “Electronic-structure of the semimetals Bi and Sb,” *Physical Review B* **52**, 1566–1577 (1995).
- [34] J. C. Y. Teo, L. Fu, and C. L. Kane, “Surface states and topological invariants in three-dimensional topological insulators: Application to  $\text{Bi}_{1-x}\text{Sb}_x$ ,” *Physical Review B* **78**, 045426 (2008).
- [35] D. Z. Hou, Z. Qiu, K. Harii, Y. Kajiwara, K. Uchida, Y. Fujikawa, H. Nakayama, T. Yoshino, T. An, K. Ando, X. F. Jin, and E. Saitoh, “Interface induced inverse spin Hall effect in bismuth/permalloy bilayer,” *Applied Physics Letters* **101**, 042403 (2012).
- [36] H. Emoto, Y. Ando, G. Eguchi, R. Ohshima, E. Shikoh, Y. Fuseya, T. Shinjo, and M. Shiraiishi, “Transport and spin conversion of multicarriers in semimetal bismuth,” *Phys. Rev. B* **93**, 174428 (2016).
- [37] Y. Fuseya, M. Ogata, and H. Fukuyama, “Spin-hall effect and diamagnetism of dirac electrons,” *J. Phys. Soc. Jpn.* **81**, 093704 (2012).
- [38] C. Sahin and M. E. Flatte, “Tunable giant spin hall conductivities in a strong spin-orbit semimetal:  $\text{Bi}_{1-x}\text{Sb}_x$ ,” *Phys. Rev. Lett.* **114**, 107201 (2015).
- [39] T. Fukazawa, H. Kohno, and J. Fujimoto, “Intrinsic and extrinsic spin hall effects of dirac electrons,” *J. Phys. Soc. Jpn.* **86**, 094704 (2017).
- [40] M. Kawaguchi, K. Shimamura, S. Fukami, F. Matsukura, H. Ohno, T. Moriyama, D. Chiba, and T. Ono, “Current-induced effective fields detected by magnetotransport measurements,” *Appl. Phys. Express* **6**, 113002 (2013).
- [41] C. O. Avci, K. Garello, M. Gabureac, A. Ghosh, A. Fuhrer, S. F. Alvarado, and P. Gambardella, “Interplay of spin-orbit torque and thermoelectric effects in ferromagnet/normal-metal bilayers,” *Phys. Rev. B* **90**, 224427 (2014).

- [42] Yong-Chang Lau and Masamitsu Hayashi, “Spin torque efficiency of ta, w, and pt in metallic bilayers evaluated by harmonic hall and spin hall magnetoresistance measurements,” *Japanese Journal of Applied Physics* **56**, 0802b5 (2017).
- [43] N. Roschewsky, E. S. Walker, P. Gowtham, S. Muschinske, F. Hellman, S. R. Bank, and S. Salahuddin, “Spin-orbit torque and nernst effect in bi-sb/co heterostructures,” *Phys. Rev. B* **99**, 195103 (2019).
- [44] Mathias Weiler, Matthias Althammer, Michael Schreier, Johannes Lotze, Matthias Pernpeintner, Sibylle Meyer, Hans Huebl, Rudolf Gross, Akashdeep Kamra, Jiang Xiao, Yan-Ting Chen, HuJun Jiao, Gerrit E. W. Bauer, and Sebastian T. B. Goennenwein, “Experimental test of the spin mixing interface conductivity concept,” *Physical Review Letters* **111**, 176601 (2013).
- [45] Axel Hoffmann, “Spin hall effects in metals,” *IEEE Trans. Magn.* **49**, 5172–5193 (2013).
- [46] Y. Shiomi, K. Nomura, Y. Kajiwara, K. Eto, M. Novak, K. Segawa, Y. Ando, and E. Saitoh, “Spin-electricity conversion induced by spin injection into topological insulators,” *Phys. Rev. Lett.* **113**, 196601 (2014).
- [47] L. Q. Liu, C. F. Pai, D. C. Ralph, and R. A. Buhrman, “Magnetic oscillations driven by the spin hall effect in 3-terminal magnetic tunnel junction devices,” *Phys. Rev. Lett.* **109**, 186602 (2012).
- [48] Q. M. Shao, G. Q. Yu, Y. W. Lan, Y. M. Shi, M. Y. Li, C. Zheng, X. D. Zhu, L. J. Li, P. K. Amiri, and K. L. Wang, “Strong rashba-edelstein effect-induced spin-orbit torques in monolayer transition metal dichalcogenide/ferromagnet bilayers,” *Nano Lett.* **16**, 7514–7520 (2016).
- [49] Yongxi Ou, Chi-Feng Pai, Shengjie Shi, D. C. Ralph, and R. A. Buhrman, “Origin of fieldlike spin-orbit torques in heavy metal/ferromagnet/oxide thin film heterostructures,” *Phys. Rev.*

- B **94**, 140414 (2016).
- [50] W. M. Yim and A. Amith, “Bi-sb alloys for magneto-thermoelectric and thermomagnetic cooling,” *Solid-State Electronics* **15**, 1141 (1972).
- [51] B. Lenoir, H. Scherrer, and T. Caillat, “Chapter 4 an overview of recent developments for BiSb Alloys,” in *Recent Trends in Thermoelectric Materials Research I*, Semiconductors and Semimetals, Vol. 69, edited by Terry M. Tritt (Elsevier, 2001) pp. 101 – 137.
- [52] J. C. Y. Teo, L. Fu, and C. L. Kane, “Surface states and topological invariants in three-dimensional topological insulators: Application to  $\text{Bi}_2\text{X}_3$ ,” *Phys. Rev. B* **78**, 045426 (2008).
- [53] Z. W. Zhu, B. Fauque, K. Behnia, and Y. Fuseya, “Magnetoresistance and valley degree of freedom in bulk bismuth,” *Journal of Physics: Condensed Matter* **30**, 313001 (2018).
- [54] J. P. Michenaud and J. P. Issi, “Electron and hole transport in bismuth,” *Journal of Physics Part C Solid State Physics* **5**, 3061 (1972).
- [55] O. Oktu and G. A. Saunders, “Galvanomagnetic properties of single-crystal antimony between 77 k and 273 k,” *Proceedings of the Physical Society of London* **91**, 156 (1967).
- [56] Junyeon Kim, Jaivardhan Sinha, Seiji Mitani, Masamitsu Hayashi, Saburo Takahashi, Sadamichi Maekawa, Michihiko Yamanouchi, and Hideo Ohno, “Anomalous temperature dependence of current-induced torques in  $\text{CoFeB}/\text{MgO}$  heterostructures with ta-based underlayers,” *Phys. Rev. B* **89**, 174424 (2014).
- [57] W. K. Tse and S. Das Sarma, “Spin hall effect in doped semiconductor structures,” *Phys. Rev. Lett.* **96**, 056601 (2006).
- [58] Edurne Sagasta, Yasutomo Omori, Miren Isasa, Martin Gradhand, Luis E. Hueso, Yasuhiro Niimi, YoshiChika Otani, and Felix Casanova, “Tuning the spin hall effect of pt from the moderately dirty to the superclean regime,” *Phys. Rev. B* **94**, 060412 (2016).

- [59] G. Y. Guo, S. Murakami, T. W. Chen, and N. Nagaosa, “Intrinsic spin hall effect in platinum: First-principles calculations,” *Phys. Rev. Lett.* **100**, 096401 (2008).
- [60] K. Uchida, S. Takahashi, K. Harii, J. Ieda, W. Koshibae, K. Ando, S. Maekawa, and E. Saitoh, “Observation of the spin seebeck effect,” *Nature* **455**, 778–781 (2008).
- [61] X. D. Xu, K. Mukaiyama, S. Kasai, T. Ohkubo, and K. Hono, “Impact of boron diffusion at mgo grain boundaries on magneto transport properties of mgo/cofeb/w magnetic tunnel junctions,” *Acta Materialia* **161**, 360–366 (2018).
- [62] S. Ikeda, K. Miura, H. Yamamoto, K. Mizunuma, H. D. Gan, M. Endo, S. Kanai, J. Hayakawa, F. Matsukura, and H. Ohno, “A perpendicular-anisotropy cofeb-mgo magnetic tunnel junction,” *Nat. Mater.* **9**, 721–724 (2010).
- [63] J. Sinha, M. Hayashi, A. J. Kellock, S. Fukami, M. Yamanouchi, M. Sato, S. Ikeda, S. Mitani, S. H. Yang, S. S. P. Parkin, and H. Ohno, “Enhanced interface perpendicular magnetic anisotropy in Ta|CoFeB|MgO using nitrogen doped Ta underlayers,” *Applied Physics Letters* **102**, 242405 (2013).
- [64] Junyeon Kim, Peng Sheng, Saburo Takahashi, Seiji Mitani, and Masamitsu Hayashi, “Spin Hall magnetoresistance in metallic bilayers,” *Physical Review Letters* **116**, 097201 (2016).
- [65] S. Cho, S. H. C. Baek, K. D. Lee, Y. Jo, and B. G. Park, “Large spin hall magnetoresistance and its correlation to the spin-orbit torque in w/cofeb/mgo structures,” *Scientific Reports* **5**, 14668 (2015).
- [66] M. N. Ali, J. Xiong, S. Flynn, J. Tao, Q. D. Gibson, L. M. Schoop, T. Liang, N. Hal-  
dolaarachchige, M. Hirschberger, N. P. Ong, and R. J. Cava, “Large, non-saturating magne-  
toresistance in wte<sub>2</sub>,” *Nature* **514**, 205 (2014).

- [67] Y. Wang, P. Deorani, X. P. Qiu, J. H. Kwon, and H. S. Yang, “Determination of intrinsic spin hall angle in pt,” *Appl. Phys. Lett.* **105**, 152412 (2014).
- [68] K. S. Lee, S. W. Lee, B. C. Min, and K. J. Lee, “Thermally activated switching of perpendicular magnet by spin-orbit spin torque,” *Appl. Phys. Lett.* **104**, 072413 (2014).
- [69] C. F. Pai, L. Q. Liu, Y. Li, H. W. Tseng, D. C. Ralph, and R. A. Buhrman, “Spin transfer torque devices utilizing the giant spin hall effect of tungsten,” *Appl. Phys. Lett.* **101**, 122404 (2012).
- [70] K. Garello, F. Yasin, S. Couet, L. Souriau, J. Swerts, S. Rao, S. Van Beek, W. Kim, E. Liu, S. Kundu, D. Tsvetanova, K. Croes, N. Jossart, E. Grimaldi, M. Baumgartner, D. Crotti, A. Fumemont, P. Gambardella, and G. S. Kar, “Sot-mram 300nm integration for low power and ultrafast embedded memories,” 2018 IEEE Symposium on VLSI Circuits , 81–82 (2018).